LETTER

https://doi.org/10.1038/s41586-018-0208-x

Extensive retreat and re-advance of the West Antarctic Ice Sheet during the Holocene

J. Kingslake[1,6]*, R. P. Scherer[2,6], T. Albrecht[3,6], J. Coenen[2], R. D. Powell[2], R. Reese[3], N. D. Stansell[2], S. Tulaczyk[4], M. G. Wearing[1] & P. L. Whitehouse[5]

To predict the future contributions of the Antarctic ice sheets to sea-level rise, numerical models use reconstructions of past ice-sheet retreat after the Last Glacial Maximum to tune model parameters[1]. Reconstructions of the West Antarctic Ice Sheet have assumed that it retreated progressively throughout the Holocene epoch (the past 11,500 years or so)[2–4]. Here we show, however, that over this period the grounding line of the West Antarctic Ice Sheet (which marks the point at which it is no longer in contact with the ground and becomes a floating ice shelf) retreated several hundred kilometres inland of today's grounding line, before isostatic rebound caused it to re-advance to its present position. Our evidence includes, first, radiocarbon dating of sediment cores recovered from beneath the ice streams of the Ross Sea sector, indicating widespread Holocene marine exposure; and second, ice-penetrating radar observations of englacial structure in the Weddell Sea sector, indicating ice-shelf grounding. We explore the implications of these findings with an ice-sheet model. Modelled re-advance of the grounding line in the Holocene requires ice-shelf grounding caused by isostatic rebound. Our findings overturn the assumption of progressive retreat of the grounding line during the Holocene in West Antarctica, and corroborate previous suggestions of ice-sheet re-advance[5]. Rebound-driven stabilizing processes were apparently able to halt and reverse climate-initiated ice loss. Whether these processes can reverse present-day ice loss[6] on millennial timescales will depend on bedrock topography and mantle viscosity—parameters that are difficult to measure and to incorporate into ice-sheet models.

Recent evidence suggests that migration of the grounding line in some areas of West Antarctica during the Holocene was more complex than previously assumed[5,7,8]. In the Weddell and Ross Sea sectors, anomalies in radar-observed englacial structure[9,10] and isostatic rebound rates[5] suggest that the grounding line was recently upstream of its present location. Rebound has been suggested to be a negative feedback on ice-sheet retreat[11–14] and a possible cause of grounding-line re-advance[5], via the grounding of ice shelves[15,16]. Better constraints on grounding-line history are important. If this history differs substantially from often-used ice-sheet reconstructions[2] over wide areas, then better constraints on past changes could lead to improved ice-sheet models[1] and measurements of ice-sheet mass change[17]. To this end, we present new evidence—from subglacial sediments and radar-observed englacial structure—for widespread re-advance of the grounding line in West Antarctica during the Holocene.

Boreholes drilled at multiple locations on the West Antarctic Ice Sheet (WAIS)—the Ross Ice Shelf Project (RISP), the Whillans Ice Stream Grounding Zone (WGZ), the Whillans Ice Stream (WIS/UpB), Subglacial Lake Whillans (SLW), the Kamb Ice Stream (KIS) and the Bindschadler Ice Stream (BIS)[18]—allowed recovery of subglacial sediments (till) up to 200 km inland of the present Ross Sea sector grounding line (Fig. 1). Radiocarbon analyses of 36 till samples indicate the widespread presence of young organic carbon stratigraphically distributed through the upper metre(s) of till. The total organic carbon concentration is low, ranging from 0.2% to 0.4%, most of which is derived from Tertiary marine deposits[19]. Nevertheless, the organic carbon in all subglacial sediments analysed includes readily measurable radiocarbon (Extended Data Table 1).

What could be the source of this young radiocarbon? Basal melting of meteoric ice is a negligible source of radiocarbon to the subglacial environment (see Methods). Subglacial microbes cannot introduce young carbon, as they rely on legacy carbon (Methods). The samples are very unlikely to have been contaminated by modern carbon, because they were curated and sealed in different laboratories, yet yielded consistent results. Hydropotential gradients[20] and high basal water pressures[18] drive subglacial water towards the grounding line in this region, eliminating the possibility of subglacial transport of ^{14}C-bearing materials from the ocean to the core sites. However, observations of an active marine community just downstream of today's grounding line—more than 600 km from the open ocean (WGZ, Fig. 1; Methods)—demonstrate that radiocarbon is introduced nearly everywhere that ocean waters reach beneath the ice shelf.

We conclude that a small proportion of the organic carbon contained in the sediments was laid down under sub-ice-shelf conditions at, or upstream of, the sediment cores recently enough to allow the persistence of measurable radiocarbon. This implies that the Siple–Gould Coast grounding line was at least 200 km inland of its present position sometime after the Last Glacial Maximum (LGM). Our calculated radiocarbon ages (Extended Data Table 1) are probably much older than the most recent marine incursion, owing to dilution by more abundant radiocarbon-dead material[4] (Methods). Moreover, ice flow transports till downstream[18], so the grounding line may have retreated even farther inland than the core sites (Fig. 1). The proximity of radiocarbon-bearing sub-ice-stream sediments to Siple Dome (SD; Fig. 1) suggests a potential correlation with around 350 m of ice-sheet thinning during the early Holocene, documented in the Siple Dome Ice Core[21].

On the other side of the WAIS, we conducted a 700-km-long, ground-based, ice-penetrating radar survey of Henry Ice Rise (HIR; Figs. 1, 2 and Methods). HIR is 7,000 km^2 in area and is grounded 310–800 m below sea level. Our survey revealed englacial structures that are inconsistent with present-day slow (less than 10 m per year) and cold-based flow conditions (see Methods).

A series of steep englacial reflectors (Fig. 2d) cluster around a basal topographic high at the northern end of HIR (Fig. 2a). These features intercept the bed, penetrate to 200–300 m above the bed, and cross-cut smoothly undulating isochrones (Fig. 2d and Extended Data Fig. 1). They have similar lateral extents, orientations and spacing to extensional surface crevasses at Doake Ice Rumples (DIR; Fig. 1 and Extended Data Fig. 2). At ice rumples, ice that was floating upstream flows onto and over a bedrock high. We interpret the buried features in HIR as marine-ice-filled relic crevasses that formed when ice-rumple flow persisted on HIR. The crevasses were probably near-vertical while active and have been buried and deformed to varying

---

[1] Lamont-Doherty Earth Observatory, Columbia University, New York, NY, USA. [2] Department of Geology and Environmental Geosciences, Northern Illinois University, DeKalb, IL, USA. [3] Potsdam Institute for Climate Impact Research (PIK), Member of the Leibniz Association, Potsdam, Germany. [4] Earth and Planetary Sciences Department, University of California Santa Cruz, Santa Cruz, CA, USA. [5] Department of Geography, Durham University, Durham, UK. [6] These authors contributed equally: J. Kingslake, R. P. Scherer, T. Albrecht. *e-mail: jkingslake@columbia.edu

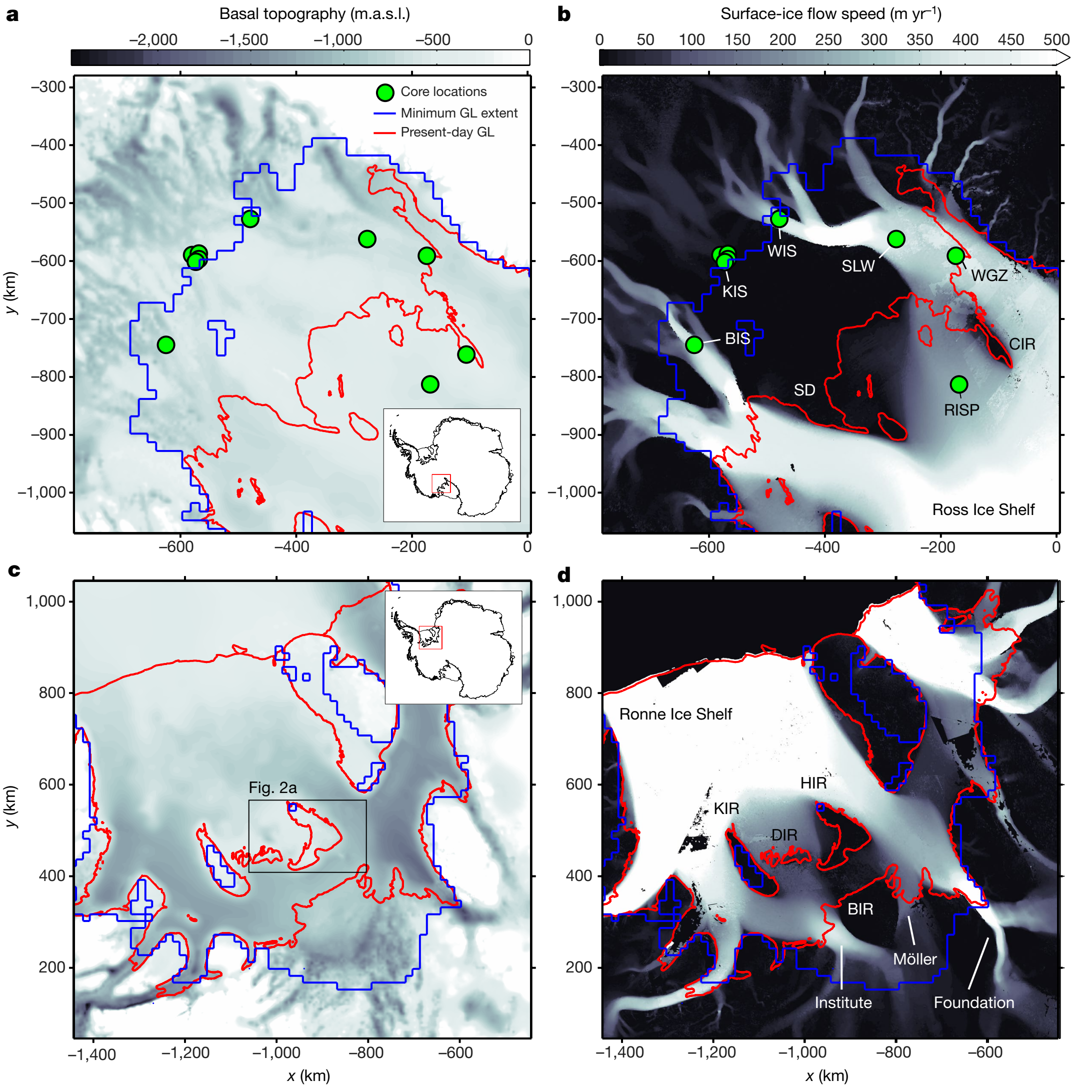

Fig. 1 | Basal topography and surface ice-flow speed in the Weddell and Ross Sea sectors of West Antarctica. a, Basal topography and bathymetry[29] and **b**, surface-ice flow speed[30] in the Ross Sea sector. The locations of sediment recovery are shown in green. m.a.s.l., metres above sea level. **c**, Basal topography and bathymetry[29] and **d**, surface-ice flow speed[30] in the Weddell Sea sector. In all panels the present-day grounding line (GL)[31] is in red, while the (asynchronous) modelled minimum extent of the grounding line in each sector is in blue. Axes show polar stereographic coordinates in kilometres. Insets show locations in West Antarctica. The Institute, Möller and Foundation ice streams are labelled.

extents into steeply dipping structures by complex ice flow (Methods). Further evidence that parts of HIR were previously floating include prominent synclines in internal isochronal layers that increase in amplitude with depth, are unrelated to basal topography and truncate at the bed (Fig. 2b, c and Extended Data Fig. 1)—characteristics indicative of past ocean melting[9].

Ice-shelf grounding on the topographic high beneath HIR—first forming ice rumples, then thickening to form the ice rise—can explain the unusual englacial structures. Contact with the ocean generates isochrone synclines where melting is focused at a static grounding line for long enough[22]. Ice-rumple flow generates surface crevasses similar to those observed on and downstream of DIR, which were preserved in HIR as flow stagnated. Prior to grounding, the ice shelf probably flowed approximately northward in the location of HIR. Post-grounding thickening upstream of the topographic high explains today's configuration, with the initial grounding point beneath HIR's northern extreme. An alternative interpretation is that HIR persisted throughout the Holocene and recently grew to its present size. However, we argue that complete ungrounding is more likely (see Methods). Under either scenario, we interpret a contrast in surface texture, approximately coincident with the onset of relic crevassing (Fig. 2b), as a signature of a past grounding-line configuration (Methods). The formation or regrowth of HIR is expected to have increased the buttressing force exerted by the Ronne Ice Shelf on the upstream ice sheet, with implications for grounding-line migration and mass balance.

To explore the cause and implications of ice-rise formation (revealed by radar observations) and ice stream grounding-line retreat and re-advance (revealed by radiocarbon analyses), we turned to numerical ice-sheet modelling. We simulated the post-LGM evolution of the WAIS using the Parallel Ice Sheet Model (PISM)[23] with improved descriptions of sub-shelf melting and solid Earth rebound, forced by sea-level and ice-core temperature reconstructions (see Methods). A model ensemble investigated first-order sensitivities to independent variations in parameters related to ice flow, glacial isostatic adjustment (GIA), calving, sub-shelf melting, basal traction and accumulation.

After partially compensating for uncertainty in bed topography (Methods), our simulations display remarkable agreement with the conclusions of our radiocarbon and radar analyses. Our reference simulation (Methods) demonstrates this agreement (Fig. 3 and Supplementary Video 1). In this simulation, rising sea-level and surface temperatures during the last glacial termination drive grounding-line retreat through regions currently occupied by the Ronne and Ross ice shelves. The grounding line reaches its most retreated position around 10 thousand years (kyr) before present (BP), up to approximately

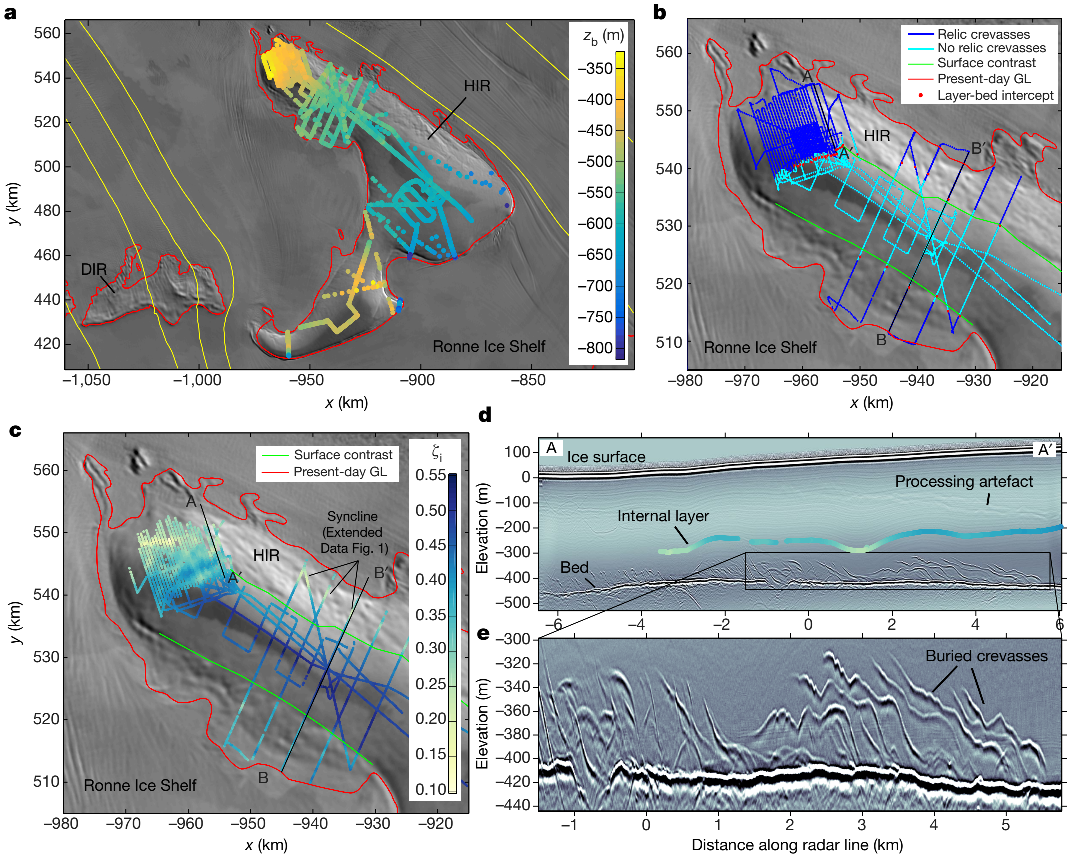

Fig. 2 | Ice-penetrating radar evidence for grounding of the Ronne Ice Shelf. a, Radar-derived ice-bed elevation beneath HIR. See Fig. 1c for location in the Weddell Sea sector. The present-day GL[31] is in red. **b**, Radar lines coloured according to where relic crevasses are found. **c**, Normalized elevation (ζ_i) of an isochrone (Methods). Background images in **a**–**c** are from the MODIS mosaic of optical (red band) imagery over Antarctica (MOA), which reveals Antarctic surface morphology[32]. Green lines in **b** and **c** highlight a contrast in surface texture (see Methods) that runs parallel to the present-day grounding line (GL), to the onset of relic crevassing and, on the east side, to a prominent isochrone syncline. **d**, Radargram displaying examples of undulating isochrones. One isochrone is mapped using the colour map from **c**. **e**, Close-up view of near-bed relic crevasses with mean spacing of approximately 450 m.

300 km inland of the present-day grounding line (Fig. 3 and Extended Data Fig. 3). Retreat exposes nearly all of our core sites and the bed of HIR to the ocean. Approximately 352,000 km^2 of the area that is covered by grounded ice today ungrounds during retreat, resulting in lithospheric rebound of up to 175 mm per year. The rising bed eventually causes the Ross and Ronne ice shelves to ground on bathymetric highs in the locations of present-day ice rises, including HIR. Ice-rise formation increases ice-shelf buttressing, causing the grounding line to re-advance towards its present-day location (Fig. 3 and Extended Data Fig. 4; Methods). In the Amundsen Sea sector, the grounding line retreats to its modern position without substantial inland retreat and re-advance.

During this simulation, rebound-driven re-advance causes the WAIS to gain ice above the flotation level equivalent to 33 cm of sea-level fall (Weddell sector, 2 cm; Ross sector, 31 cm). Ice-volume minima in each sector are asynchronous and the minimum in whole ice-sheet volume occurs 1.5 kyr BP, at which time the ice sheet is 20 cm sea-level equivalent smaller than at present.

The timing and magnitude of the simulated grounding-line retreat and re-advance depend on model parameters, forcings, bed topography and spatial resolution (Extended Data Figs. 6 and 7; Methods). For example, increasing mantle viscosity expedites retreat, increases maximum retreat and delays re-advance. Ice-rise formation greatly enhances grounding-line re-advance and is sensitive to bed topography, which is regionally uncertain; moreover, dynamically relevant topographic features are poorly represented at the spatial resolution of the model (Extended Data Fig. 4 and Methods).

Notably, although grounding-line re-advance was not their focus, four previous Antarctic ice-sheet modelling studies—using alternative parameterizations of basal sliding, grounding-line flux and lithosphere response—also simulate Holocene grounding-line retreat and re-advance in these sectors in some simulations[24–27].

Radiocarbon in subglacial sediments, radar-observed relic crevassing and ice-sheet modelling provide corroborating evidence that two large Antarctic catchments re-advanced to their present-day configurations during the Holocene (Fig. 3). Previous work is consistent with this conclusion, but cannot confirm or rule out Holocene retreat and re-advance (see Methods). Moreover, previous authors have found evidence for localized re-advance and suggested rebound as a cause[5,10]. However, ice-sheet reconstructions used to tune ice-sheet models and to correct mass-balance observations do not at present include large-scale grounding-line re-advance[1,2]. Updating these reconstructions to include re-advance could influence ice-sheet gravimetry and altimetry[17], and sea-level projections. Furthermore, we hypothesize that the grounding line in the Weddell and Ross Sea sectors may be capable of retreating far inland of its present position without triggering runaway ice-sheet collapse.

We note that our model does not simulate retreat and rebound-driven re-advance in the Amundsen Sea sector (Fig. 3), where present-day retreat of the grounding line is causing concern about future runaway collapse[6] and recent re-advance could explain observed sub-shelf iceberg ploughmarks[28]. Our findings motivate future work to examine whether rebound-driven mechanisms could slow or reverse this retreat on millennial timescales.

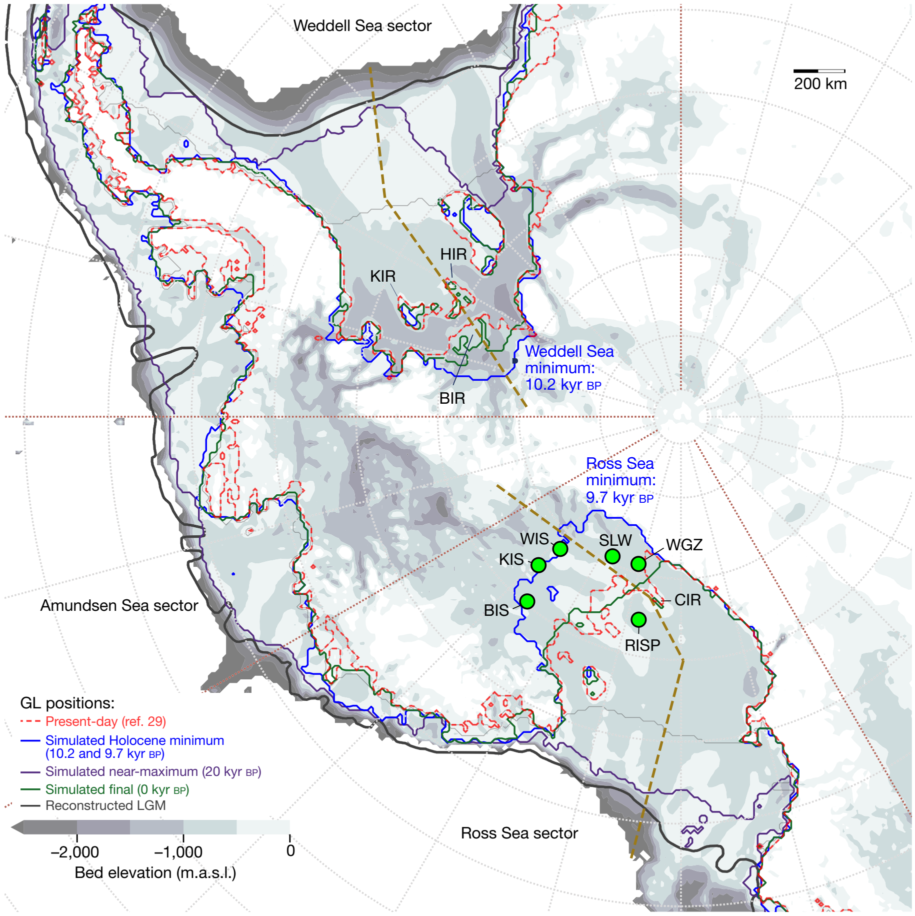

Fig. 3 | Modelled grounding-line retreat and re-advance due to lithospheric rebound. The position of the WAIS grounding line at 20 kyr BP in our reference simulation is shown in violet, with a recent LGM ice-sheet reconstruction in black (ref. [2], scenario B). The ice sheet asynchronously reaches a minimal extent in the Weddell and Ross Sea sectors at 10.2 kyr BP and 9.7 kyr BP respectively (blue). The grounding line (GL) then re-advances towards its present-day location[29] (red). The final simulated grounding-line position is in green. The locations of Siple–Gould Coast sediment cores and selected ice rises are indicated. Brown dashed lines show cross-sections used for Extended Data Figs. 3, 6 and 7. Red dotted lines show longitude-defined sectors. Background shading shows basal topography and bathymetry[29].

Rising eustatic sea levels and temperatures were major climate-related drivers of ice-sheet retreat during and after the last glacial termination. By contrast, it appears that climate-independent lithospheric rebound and ice-shelf grounding were the main drivers of grounding-line re-advance during the Holocene. The impact of rebound on the ice sheet depends sensitively on bedrock topography and mantle viscosity (see Methods). Accurate mapping of potential grounding points and improved parameterization of uplift are needed to forecast the direction and rate of future grounding-line migration in West Antarctica.

Online content

Any Methods, including any statements of data availability and Nature Research reporting summaries, along with any additional references and Source Data files, are available in the online version of the paper at https://doi.org/10.1038/s41586-018-0208-x.

Received: 30 August 2017; Accepted: 28 March 2018;
Published online: 13 June 2018

1. DeConto, R. M. & Pollard, D. Contribution of Antarctica to past and future sea-level rise. *Nature* **531**, 591–597 (2016).
2. Bentley, M. J. et al. A community-based geological reconstruction of Antarctic Ice Sheet deglaciation since the Last Glacial Maximum. *Quat. Sci. Rev.* **100**, 1–9 (2014).
3. Conway, H. et al. Past and future grounding-line retreat of the West Antarctic Ice Sheet. *Science* **286**, 280–283 (1999).
4. Spector, P. et al. Rapid early-Holocene deglaciation in the Ross Sea, Antarctica. *Geophys. Res. Lett.* **44**, 7817–7825 (2017).
5. Bradley, S. L. et al. Low post-glacial rebound rates in the Weddell Sea due to Late Holocene ice-sheet readvance. *Earth Planet. Sci. Lett.* **413**, 79–89 (2015).
6. Scambos, T. A. et al. How much, how fast? A science review and outlook for research on the instability of Antarctica's Thwaites Glacier in the 21st century. *Global Planet. Change* **153**, 16–34 (2017).
7. Goodwin, I. D. Did changes in Antarctic ice volume influence late Holocene sea-level lowering? *Quat. Sci. Rev.* **17**, 319–332 (1998).
8. Halberstadt, A. R. W., Simkins, L. M., Greenwood, S. L. & Anderson, J. B. Past ice-sheet behaviour: retreat scenarios and changing controls in the Ross Sea, Antarctica. *Cryosphere* **10**, 1003–1020 (2006).
9. Catania, G. A. et al. Evidence for floatation or near floatation in the mouth of Kamb Ice Stream, West Antarctica, prior to stagnation. *J. Geophys. Res. Earth Surf.* **111**, F01005 (2006).
10. Siegert, M. et al. Late Holocene ice-flow reconfiguration in the Weddell Sea sector of West Antarctica. *Quat. Sci. Rev.* **78**, 98–107 (2013).
11. Adhikari, S. et al. Future Antarctic bed topography and its implications for ice sheet dynamics. *Solid Earth* **5**, 569–584 (2014).
12. Gomez, N., Pollard, D. & Holland, D. Sea-level feedback lowers projections of future Antarctic Ice-Sheet mass loss. *Nat. Commun.* **6**, 8798 (2015).
13. Greischar, L. L. & Bentley, C. R. Isostatic equilibrium grounding line between the West Antarctic inland ice sheet and the Ross Ice Shelf. *Nature* **283**, 651–654 (1980).
14. Konrad, H. et al. Potential of the solid-Earth response for limiting long-term West Antarctic Ice Sheet retreat in a warming climate. *Earth Planet. Sci. Lett.* **432**, 254–264 (2015).
15. Matsuoka, K. et al. Antarctic ice rises and rumples: their properties and significance for ice-sheet dynamics and evolution. *Earth Sci. Rev.* **150**, 724–745 (2015).
16. Thomas, R. H. The creep of ice shelves: interpretation of observed behavior. *J. Glaciol.* **12**, 55–70 (1973).
17. Hanna, E. et al. Ice-sheet mass balance and climate change. *Nature* **498**, 51–59 (2013).
18. Kamb, B. in *The West Antarctic Ice Sheet: Behavior and Environment* (eds Alley, R. B. & Bindschadler, R. A.) 157–199 (American Geophysical Union, Washington DC, 2001).

19. Scherer, R. P. Quaternary and tertiary microfossils from beneath ice stream B: evidence for a dynamic West Antarctic ice sheet history. *Palaeogeogr. Palaeoclimatol. Palaeoecol*. **90**, 395–412 (1991).
20. Livingstone, S. et al. Potential subglacial lake locations and meltwater drainage pathways beneath the Antarctic and Greenland ice sheets. *Cryosphere* **7**, 1721–1740 (2013).
21. Price, S. F., Conway, H. & Waddington, E. D. Evidence for late Pleistocene thinning of Siple Dome, West Antarctica. *J. Geophys. Res. Earth Surf*. **112**, F03021 (2007).
22. Catania, G., Hulbe, C. & Conway, H. Grounding-line basal melt rates determined using radar-derived internal stratigraphy. *J. Glaciol*. **56**, 545–554 (2010).
23. Winkelmann, R. et al. The Potsdam Parallel Ice Sheet Model (PISM-PIK)—part 1: model description. *Cryosphere* **5**, 715–726 (2011).
24. Pollard, D. et al. Large ensemble modeling of the last deglacial retreat of the West Antarctic Ice Sheet: comparison of simple and advanced statistical techniques. *Geosci. Model Dev*. **9**, 1697–1723 (2016).
25. Golledge, N. R. et al. Antarctic contribution to meltwater pulse 1A from reduced Southern Ocean overturning. *Nat. Commun*. **5**, 5107 (2014).
26. Maris, M. N. A. et al. A model study of the effect of climate and sea-level change on the evolution of the Antarctic Ice Sheet from the Last Glacial Maximum to 2100. *Clim. Dyn*. **45**, 837–851 (2015).
27. Pollard, D., Gomez, N. & Deconto, R. M. Variations of the Antarctic ice sheet in a coupled ice sheet-Earth-sea level model: sensitivity to viscoelastic Earth properties. *J. Geophys. Res. Earth Surf*. **122**, 2124–2138 (2017).
28. Graham, A. G. et al. Seabed corrugations beneath an Antarctic ice shelf revealed by autonomous underwater vehicle survey: origin and implications for the history of Pine Island Glacier. *J. Geophys. Res. Earth Surf*. **118**, 1356–1366 (2013).
29. Fretwell, P. et al. Bedmap2: improved ice bed, surface and thickness datasets for Antarctica. *Cryosphere* **7**, 375–393 (2013).
30. Rignot, E., Mouginot, J. & Scheuchl, B. Ice flow of the Antarctic ice sheet. *Science* **333**, 1427–1430 (2011).
31. Depoorter, M. A. et al. Calving fluxes and basal melt rates of Antarctic ice shelves. *Nature* **502**, 89–92 (2013).
32. Haran, T. et al. MODIS mosaic of Antarctica 2003–2004 (MOA2004) image map. *US Antarctic Program Data Center* https://doi.org/10.7265/N5ZK5DM5 (2005).

Acknowledgements J.K. and the Weddell Sea fieldwork were funded by Natural Environmental Research Council (NERC) grant NE/J008087/1, led by R. Hindmarsh. Logistical support was provided by many members of the British Antarctic Survey's air unit and field operations team. We particularly thank I. Rudkin and S. Webster for assistance in the field. We also thank H. Pritchard for supplying bed elevation data and Schlumberger Limited for a software donation. PISM development is supported by NASA grants NNX13AM16G and NNX13AK27G. T.A. is supported by the Deutsche Forschungsgemeinschaft (DFG) in the framework of the priority program 'Antarctic Research with comparative investigations in Arctic ice areas' through grants LE1448/6-1 and LE1448/7-1.We acknowledge the European Regional Development Fund, the German Federal Ministry of Education and Research, and the Land Brandenburg for providing high-performance computer resources at the Potsdam Institute for Climate Impact Research. We also thank the Gauss Centre for Supercomputing e.V. (http://www.gauss-centre.eu) for providing computing time on the GCS Supercomputer SuperMUC at Leibniz Supercomputing Centre (http://www.lrz.de; project code pr94ga). We thank C. Buizert for providing ice-core temperature reconstructions; D. Peltier for access to eustatic sea-level reconstructions; J. Lenaerts for surface mass balance data from the RACMO climate model; and S. Jamieson for providing the RAISED consortium's grounding-line reconstructions. R.P.S., J.C., R.D.P. and S.T. were funded by National Science Foundation (NSF) WISSARD Project grants ANT-0839107, ANT-0839142, ANT-0838947 and ANT-0839059. Collection of subglacial sediment samples at Subglacial Lake Whillans and the Whillans Grounding Zone was facilitated by the US Antarctic Program and the efforts of multiple field support teams, including the drilling team from the University of Nebraska–Lincoln and WISSARD traverse personnel, as well as by Air National Guard and Kenn Borek Air who provided air support. WIS, KIS and BIS samples were recovered by B. Kamb's program at the California Institute of Technology (1988–2001), which included R.P.S. and S.T.; samples from the US Antarctic Program's Ross Ice Shelf Project (1977–1979) cores were made available for study by the US Antarctic Sediment Core Repository, Florida State University. P.L.W. is funded by a NERC Independent Research Fellowship (NE/K009958/1). This research is a contribution to the Scientific Committee on Antarctic Research (SCAR) Solid Earth Response and Influence on Cryosphere Evolution (SERCE) program. We thank R. Arthern, R. Bell, R. Hindmarsh, C. Martín, J. Southon and K. Tinto for discussions that contributed to this study. We particularly thank D. Pollard for sharing ideas and unpublished Penn State model outputs for discussion.

Reviewer information *Nature* thanks R. Drews, J. Smith and the other anonymous reviewer(s) for their contribution to the peer review of this work.

Author contributions All authors contributed to manuscript preparation. T.A., J.K. and R.P.S. are co-lead authors with equal contributions; others are listed alphabetically. J.K. designed and conducted the Weddell Sea sector ice-penetrating radar survey and led the preparation of the manuscript. R.P.S., J.C., R.D.P. and S.T. collected and analysed sub-ice sediment samples as part of the WISSARD and earlier drilling projects in the Ross Sea sector. N.D.S. and J.C. prepared samples and interpreted ^{14}C and ^{13}C results. T.A. ran the PISM simulations and an extended analysis of parameter sensitivity. R.R. designed and analysed experiments for disentangling drivers of re-advance. M.G.W. analysed radar data from the Weddell Sea sector. P.L.W. provided input on parameterization of solid-Earth rebound and sea-level forcing for the model experiments.

Competing interests The authors declare no competing interests.

Additional information

Extended data is available for this paper at https://doi.org/10.1038/s41586-018-0208-x.
Supplementary information is available for this paper at https://doi.org/10.1038/s41586-018-0208-x.
Reprints and permissions information is available at http://www.nature.com/reprints.
Correspondence and requests for materials should be addressed to J.K.

METHODS

Sediments. *Radiocarbon and ^{13}C analyses of glacial tills.* Subglacial sediments have been recovered during multiple field seasons by hot-water drilling through the southern Ross Ice Shelf and grounded West Antarctic Ice Sheet. Sub-ice-shelf core samples include the Ross Ice Shelf Project (RISP, 1978; ref. [33]) and the Whillans Ice Stream Grounding Zone (WGZ, 2015), recovered as part of the Whillans Ice Stream Subglacial Access Research Drilling (WISSARD) Project. The WISSARD Project also recovered cores from beneath grounded ice at Subglacial Lake Whillans (SLW, 2013). Sub-ice-stream samples further upstream were recovered from the Whillans (WIS/UpB, 1989, 1991, 1995, SLW, 2013), Kamb (KIS, 1995, 1996, 2000) and Bindschadler (BIS, 1998) ice streams[18]. The sediments recovered are tills with a matrix derived in part from strata that accumulated during multiple intervals of terrestrial, coastal and open marine deposition in West Antarctica. Source strata integrated into the tills are dated by microfossils[19,34]. They include terrestrial plant spores dating back to the Devonian, but are dominantly Miocene-age diatoms, reflecting the abundance of Miocene marine strata in the embayment. The youngest diatoms present are of Pleistocene age, representing direct precipitation in open water during intervals of past ice-sheet collapse during Marine Isotope Stage 5e (MIS-5e; 120 kyr BP) or earlier Pleistocene interglacials[35]. These microfossils predate any measurable radiocarbon source in the sub-glacial environment.

Bulk sediment samples for radiocarbon measurements were wet sieved with nanopure water through a 63-μm screen to remove coarser mineral matter, then pre-treated using standard acid–base–acid protocols[36]. The remaining insoluble fraction for each sample was combusted to convert to CO_2 and then graphitized. Samples were then measured using accelerator mass spectrometry at the WM Keck Carbon Cycle Laboratory at the University of California, Irvine. A subset of samples was also independently pre-treated and measured at the Uppsala radiocarbon facility, Sweden, following the same protocol. Owing to the inherent age uncertainties, radiocarbon 'ages' are presented as raw, uncalibrated values that are not corrected for known reservoir effects. Acid-insoluble organic ^{13}C ratios were generated separately at the Environmental Isotope Laboratory at the University of Arizona, following standard methods.

In order to minimize the potential for contamination of small samples during analysis, we processed large samples (larger than 150 mg), producing around 1 mg to 2 mg of carbon that was combusted and reduced to graphite, while simultaneously processing numerous primary and secondary standards, ranging in size from very small (less than 0.1 mg) to large (1.8 mg). To further demonstrate that we have thoroughly explored a wide range of radiocarbon systematics, we also dated base-soluble fractions for a subset of samples. The base-soluble fraction (humic acid) resulted in ages that were somewhat older (about 1–2 kyr old) than the bulk sediment samples. These age differences are relatively small and the results are consistent with our other findings. Multiple fractions that yield similar ages further rule out contamination as a possible explanation of our radiocarbon results.

We considered and ruled out sample contamination by modern carbon before analysis as a potential explanation of the radiocarbon results. Subglacial samples were recovered between 1989 and 2013, and sub-ice-shelf samples were recovered in 2015 (WGZ) and 1978 (RISP). SLW (2013) samples were recovered and handled using full clean-access protocols[37], where all instruments were peroxide washed before recovery. Cores and samples were sealed and maintained in a +4 °C environment. Clean-access protocols were not used during earlier sample recovery (for WIS, KIS and BIS), although every effort was made to maintain appropriate cleanliness in the field and in the laboratory. These samples were sealed and maintained at +4 °C. Subsamples were stored in sealed sections of plastic-core liner, in plastic bags or in plastic vials. Many of the samples in vials dried out and some of the dried samples have been stored at room temperature in the intervening years. The fact that the older subglacial samples demonstrate the oldest apparent radiocarbon ages argues against any introduction of new carbon from microbial or fungal growth on the sample. RISP cores were stored at the Florida State University Antarctic sediment-core repository, sealed and chilled. The somewhat younger ages there are readily explained by the long-term exposure to the sub-ice-shelf ocean cavity. Despite the different sample storage methods used, the radiocarbon results are very consistent, which argues against contamination. Given the small concentration of organic carbon in the samples, a very small amount of contamination with modern carbon would result in some anomalous younger ages, yet all of our results fall within a narrow range. Given the range of sample sources and storage methods, equal contamination of all the samples consistent with our results is extremely unlikely.

Apparent and true ages of sediments. Given the dominant concentration of old (radiocarbon dead) organic carbon in the samples[38], all ages presented here are older than the likely age of the pure radiocarbon component; note the calculated 'per cent modern' column in Extended Data Table 1. We infer post-LGM ages for all samples. Apparent radiocarbon ages for 11 till samples from beneath the Whillans, Kamb and Bindschadler ice streams were obtained for acid-insoluble organics (AIOs) and span from around 20 to 35 kyr BP (Extended Data Fig. 5). Rare, small biogenic carbonate fragments from molluscs, foraminifera and calcareous nanofossils have been found in several samples, but these are all Tertiary in age (on the basis of biostratigraphic assessment[19]), and we made no attempt to radiocarbon date them.

Sediments recovered from beneath the southern Ross Ice Shelf (RISP cores; Fig. 1) were radiocarbon dated, generally yielding somewhat younger ages than the ice streams, probably reflecting the longer period of contact with the sub-ice-shelf marine cavity. For the most part, the raw ages appear to correspond to the LGM of the WAIS, which started about 29 kyr BP and ended 13.9–15.2 kyr BP (ref. [39]). Many lines of geologic evidence document that the LGM grounding line of the WAIS was located at or near the Ross Sea continental shelf break[40] at the time that corresponds with the apparent, uncorrected radiocarbon ages in our samples.

For the apparent ^{14}C ages to represent the true sediment ages, the grounding line of the WAIS would have to be upstream of the core sampling locations and also require all of the carbon pool in the samples to initially have had the standard, modern $^{14}C/^{12}C$ ratio. However, owing to the large oceanic reservoir effect in Antarctica, even modern amphipods sampled by us in January 2015 through a borehole at the grounding line of Whillans Ice Stream (WGZ; Fig. 1 and Extended Data Table 1) had a fraction of modern radiocarbon of only 0.8669–0.8746, corresponding to apparent ages of 1,075–1,145 ^{14}C years. Moreover, it is well documented that radiocarbon dates on AIOs obtained from bulk Antarctic glacigenic sediments are typically biased by admixture of old, ^{14}C-depleted organic matter[4,41–43]. This old organic material comes from glacial erosion of sediments deposited earlier in the Cenozoic[34]. The tills of the Ross ice streams are dominated by Tertiary, mostly Upper Miocene[34,35], marine source beds that are being actively eroded by grounded ice[19]. Given the uncertainty concerning the initial mixture between 'young' and 'old' sources of organic matter, we know only that the true age of the radiocarbon falls somewhere along the exponential-decay lines of ^{14}C in Extended Data Fig. 5, which intersect the left-hand vertical axes of this figure at the measured values of the ^{14}C modern fraction.

Instead of the apparent ^{14}C ages representing the true sediment ages, it is more reasonable to assume that the WAIS grounding line was upstream of the till sampling locations after the LGM, and that the calculated ages are biased towards older dates owing to the high concentration of ancient carbon (Extended Data Fig. 5). Our assumption is also compatible with the relatively low initial fractions of ^{14}C in sampled sediments, which we expect given that the sampled subglacial areas were exposed to an influx of marine-sourced radiocarbon over a geologically short period of time and were located very far from the main locus of regional biological productivity in the Ross Sea. For instance, if our sediment samples had received ^{14}C-bearing marine organics in the mid-Holocene (around 5 kyr BP), then the initial fractions of ^{14}C for these samples could be quite low (roughly 0.03 to 0.14) to explain the obtained apparent ages. By contrast, if one chooses a time period pre-dating the WAIS LGM, say 30 kyr BP, then most of our samples would need to have all of their organic matter completely equilibrated with the oceanic pool of ^{14}C at that time. Such conditions are difficult to find even in the modern open marine sediments of Ross Sea[41,42].

The balance of evidence favours a post-LGM origin of ^{14}C-bearing organics in our till samples. However, the radiocarbon data do not allow us to pinpoint more precisely when the proposed retreat and re-advance of the WAIS grounding line took place in the Ross Sea sector of the ice sheet, or the specific duration of exposure.

Potential input of radiocarbon from basal melting. Here we check whether ^{14}C in subglacial sediment samples from beneath three different ice streams may have been entirely, or at least to a substantial extent, supplied by basal melting of meteoric ice. Meteoric ice may contain as much as 140 mm^3 of air per gram[44], which translates into about 0.02 g of total inorganic carbon (TIC) per m^3 of ice, assuming an ice density of 910 $kg\ m^{-3}$ and a pre-industrial Holocene atmospheric concentration of carbon dioxide (280 parts per million, p.p.m.). Meteoric ice also contains organic matter deposited from the atmosphere[45,46]. From these two publications[45,46] we select 100 μg per litre as an upper bound on the total organic carbon (TOC) concentration in ice coming from the interior of the ice sheet. This assumption yields around 0.1 g of TOC per m^3 of ice. TIC and TOC combined give 0.12 g of carbon per m^3 of meteoric glacial ice. Basal melting rates vary beneath the Ross Sea sector of the WAIS, but 0.003 m per year provides a representative estimate for the region[47]. At this rate 0.36 g of carbon per m^2 of the bed area would be entering the subglacial zone of the ice sheet in each thousand years. Some of this material would be entering subglacial sediments already as organic carbon melted out of the ice, whereas the component derived from carbon dioxide trapped in the melting ice would exist as dissolved inorganic carbon (DIC). We assume that the latter could be relatively quickly sequestered by subglacial microbial activity and converted into organic matter[48].

The basal flux of carbon estimated above needs to be compared with the total stock of carbon in the subglacial till from which our samples are derived. Our radiocarbon measurements show that ^{14}C is present at least within the top metre of till recovered from beneath three Ross Sea sector ice streams. Analyses performed in the University of California Santa Cruz stable-isotope laboratory (UCSC CF-IRMS) on 27 subglacial sediment samples show an average TOC of 0.33% (with a standard deviation of 0.14%, both expressed in weight per cent of the dry sedimentary matter). Because the dry density of the till is about 1,600 kg m^{-3} (ref. [49]), a metre-thick layer of till contains about 5 kg of organic carbon per m^3 of sediment. Even if we assume that all of the carbon entering the subglacial zone with basal meltwater is sequestered within the top metre of till, it would take about 14 million years to supply the total amount of carbon found in these sediments just from basal melting at the rate of 0.36 g per 1,000 years. Owing to ^{14}C decay, only the carbon released by basal melting during the last tens of thousands of years can contribute to the present stock of this radioisotope in till. The remaining ratio, R, of undecayed ^{14}C in a pool of carbon accumulating through time, t, by the addition of new ^{14}C-bearing matter at a constant rate can be calculated from:

$$R_{\{t\}} = \frac{R_0}{t}\int_0^t \mathrm{e}^{-\varsigma/\lambda}\mathrm{d}\varsigma = R_0\frac{\lambda}{t}(1-\mathrm{e}^{-t/\lambda})$$

where R_0 is the initial ^{14}C ratio (for example, the modern atmospheric ^{14}C /^{12}C ratio), ς is a dummy variable of integration, and $\lambda = 3{,}972$ years (a constant given as the product of ^{14}C half-life, 5,730 years, and the natural logarithm of 2). After 14 million years (Myr), the hypothetical subglacial carbon pool resulting solely from a continuous accumulation of carbon released from basal melting of meteoric ice would have an average ^{14}C ratio of only 0.00028 of its initial (for example, modern) value. This is two orders of magnitude too low to explain the fractions of ^{14}C measured in our samples. From the equation above, we can calculate that the observed fractions of ^{14}C could be explained only by constant accumulation of carbon with modern initial ^{14}C over periods of time of around 100 kyr or less. However, the flux rate of carbon from basal melting would then have to be around 50 g per thousand years per unit area of the ice base in order to explain the total stock of carbon in the sampled subglacial sediment layer (around 5 kg m^{-3}). As per our discussion above, such rates of carbon delivery from melting basal ice are implausibly high.

The analyses presented here did not even take into account the fact that any carbon released from the base of the ice streams has spent thousands to tens of thousands of years stored in the ice itself, which would further decrease its ^{14}C content. Furthermore, an ice-stream base can also be composed of basal ice that has been formed by the freezing of subglacial waters. Such basal ice would not contain ^{14}C-bearing carbon dioxide or organic matter. Hence, we conclude that the release of ^{14}C from the base of the ice sheet does not represent a substantial source, and that the inclusion of recent marine organic matter during a recent ice sheet retreat is needed to explain the concentrations of this isotope measured in our samples. Furthermore, the radiocarbon results we report are completely consistent with the ice-sheet retreat ages inferred from the radar profiles and modelling reported here.

A modern analogy from the present-day sub-shelf cavity. Hot-water drilling through 760 m of ice into 10 m of water in a sub-ice shelf-embayment more than 600 km from the open ocean, at the Whillans Ice Stream grounding zone[50] (WGZ; Fig. 1), revealed a diverse community of organisms—including diverse amphipods, zoarcid and notothenioid fishes, and medusoid and ctenophorid jellies—thriving in fully marine water. Radiocarbon analysis of appendages from three live-captured amphipods yielded raw ages between 1,075 ± 20 and 1,145 ± 20 yr BP (Extended Data Table 1), comparable to the Ross Sea surface water reservoir age[51]. The results from this grounding-line-proximal community of organisms show that radiocarbon is introduced from the open ocean virtually everywhere that ocean waters reach beneath the ice shelf. A retreating grounding line would have opened a subglacial marine environment that was immediately colonized by organisms that leave a radiocarbon tracer on their death. This modern sub-ice shelf process illustrates a likely pathway for Holocene radiocarbon to be deposited upstream of the present grounding line following past grounding-line retreat. Furthermore, pore-water chemistry indicative of seawater at Subglacial Lake Whillans (SLW; Fig. 1)[48] demonstrates that marine waters previously occupied the subglacial lake basin.

Henry Ice Rise: observations, interpretation and flow history. Henry Ice Rise (HIR) is one of several ice rises in the Weddell Sea that influence the flow of the Ronne Ice Shelf and its ice streams. It is currently slow flowing[30] and cold based[52]. On the basis primarily of new ground-based ice-penetrating radar data, we hypothesize that HIR formed during the Holocene as the Ronne Ice Shelf grounded on a bathymetric high. Here we describe the radar system and our processing steps, and discuss possible links between surface roughness and englacial structure, which pertain to a potential past grounding-line configuration. We also discuss an alternative interpretation that HIR existed throughout the Holocene, but was in the past smaller than it is today.

Radar system. We used the British Antarctic Survey's DEep LOoking Radio-Echo Sounder (DELORES) on HIR to map basal topography and englacial structure[53]. A transmitter producing 2,500 broadband radiowave pulses per second was connecting to a 20-m, resistively loaded dipole antenna, so that the centre frequency of the system in ice was 4 MHz. A receiver unit, positioned 100 m from the transmitter and connected to an identical dipole antenna, was triggered by the air wave and sampled the return signal at 250 MHz. The system was towed 50 m behind a snowmobile, driven at about 15 km h^{-1}. After stacking, this configuration produced traces roughly every 85 cm along the track.

Data processing. Traces were geolocated in three dimensions using data from a dual-band GPS unit, mounted at the midpoint of the transmitter and receiver, then interpolated onto a regularly spaced grid, bandpass filtered and compiled into radargrams. Radargrams were migrated with a two-dimensional Kirchoff scheme, assuming a constant radiowave velocity of 0.168 m ns^{-1} (ref. [53]).

Elevations of the ice-bed interface and one of many englacial reflecting horizons, interpreted as isochrones, were determined using the software package Petrel by Schlumberger. Conversion from the two-way travel time of the radar signal to depth was made assuming a constant radiowave velocity (0.168 m ns^{-1}). Correcting for the impact of the lower density of the firn on radiowave velocity would decrease the elevation by up to 10 m. As firn densities are unknown on HIR and probably vary spatially, we plot the uncorrected elevation of the ice-bed interface, z_b (Fig. 2a). Also plotted in Fig. 2a are ice-bed elevations from the BEDMAP2 dataset (H. Pritchard, personal communication). The normalized elevation of the isochrones, ζ_i, is computed from $\zeta_\mathrm{i} = (z_\mathrm{i} - z_\mathrm{b})/(z_\mathrm{s} - z_\mathrm{b})$, where z_i is the elevation of the isochrone and z_s is the ice-surface elevation measured with the dual-band GPS (Fig. 2c).

Surface-texture contrasts visible in satellite imagery and surface-elevation data. Antarctic satellite imagery can be used to reveal subtle ice-surface topography[54,55]. The MODIS Mosaic of Antarctica image in Fig. 2 highlights contrasting regions near the northern end of HIR, which we interpret as indicative of contrasting surface roughness. The green curves in Fig. 2b, c highlight the boundaries between the regions. The area between the two green curves appears smoother than the two regions between the green curves and the present-day grounding line. This interpretation is consistent with surface slopes estimated from elevation data collected by the GPS unit mounted on the DELORES radar system (data not shown).

The surface-texture contrasts are approximately parallel to the present-day grounding line and align roughly with the following features revealed by our ice-penetrating radar survey: extensive synclines in internal isochrones (Fig. 2c and Extended Data Fig. 2a), locations where isochrones intercept the bed (Fig. 2b and Extended Data Fig. 2f), and the onset of buried crevasses (Fig. 2b). Here we explain these alignments by proposing that all of these features are the signatures of a past grounding-line configuration that persisted during a period either following the grounding of the ice rise, or when HIR was at its minimum extent (see below).

Today on the ice-shelf side of the eastern grounding line of HIR, ice undergoes lateral shear as the ice shelf moves past the relatively slow ice rise. This shear generates a region of dense crevassing (Extended Data Fig. 2g). Deformation in shear margins also warms englacial ice and generates ice-crystal fabric. Both can influence the effective viscosity of ice, as can crevassing. As the grounding line swept through the region between the surface-texture contrast and the present-day grounding line, crevasses generated on the ice-shelf side would have become inactive, buried and then deformed in the slow-moving ice. Simultaneously, englacial temperatures and crystal fabrics would have evolved in a complex manner as the shear margin migrated in step with grounding-line migration. We hypothesize that these changes, together with spatially heterogeneous basal melting, resulted in the complex pattern of tilted crevasses we observe today.

Under this interpretation, the rougher surface texture in the region presently occupied by buried crevasses (Fig. 2) results from spatially variable ice viscosity caused by variability in the orientation and height of crevasses, as well as spatially variable ice fabric and temperature that have evolved enough to still affect ice flow. By contrast, the ice in the region between the two green curves (Fig. 2) has undergone a simpler flow history, without substantial lateral shearing, either because it was immediately upstream of the initial location of grounding (the subglacial high in Fig. 2a) and experienced only longitudinal compression, or because it did not unground. We discuss the latter scenario next.

An alternative interpretation: a smaller-than-present but persistent HIR. In the main text and in the previous section, we interpreted our radar observations to indicate that HIR became completely ungrounded following the LGM, then formed through regrounding on the topographic high at the northern end of HIR. However, some of our radar observations can be explained by an alternative ice-flow history. The grounding line surrounding HIR may have retreated substantially, exposing areas of the ice base to the ocean, where heterogeneous basal melting deformed and truncated isochrones at the bed. Subsequent re-advance of the grounding line would have buried crevassing as described above. This would have had an effect on regional ice-shelf dynamics and buttressing, but HIR would have persisted throughout the Holocene. However, if the locations where isochrones are truncated at the bed correspond to areas that ungrounded, then the simplest minimum extent suggested by mapping the layer truncations (Fig. 2b) would involve the ice rise ungrounding over the highest basal topography (Fig. 2a), while remaining grounded over deeper bathymetry. We do not yet understand ice-rise dynamics sufficiently to fully assess if this is possible. However, such a pattern of ungrounding during deglaciation is inconsistent with recent numerical modelling of idealized ice-rise formation[56]. Therefore, we argue that full ungrounding and later regrounding is more likely than partial ungrounding.

Whether the ice rise ungrounded completely or partially, the buttressing force exerted by the ice shelf on the ice sheet upstream would have been affected. These scenarios could be tested by drilling to the ice-rise base to obtain sediments for radiocarbon analysis and to allow measurement of the englacial temperature profile[57].

Ice-sheet modelling. *Model description and forcings.* We used the open-source Parallel Ice Sheet Model (PISM)[23,58,59] to perform pan-Antarctic simulations with glacial-cycle climate forcings. PISM is a three-dimensional, thermo-mechanically coupled ice-flow model with a freely evolving grounding line and calving front. The hybrid shallow approximation of Stokes flow allows for large-scale, long-term simulations of ice-sheet evolution. Unless otherwise stated, we used surface-temperature anomalies from the WAIS divide ice-core (WDC) reconstruction[60], which show a sharp increase of 11 K starting around 17 kyr BP. For surface accumulation, we use the 1980–2000 mean accumulation from the output of a regional climate model (RACMOv2.1, HadCM3; ref. [61]) as a base accumulation pattern and scale this pattern by 2% per degree of climatic temperature change from present[62] (using the WDC reconstruction) and by 43% per km of surface elevation change. The latter assumes a linear dependence of air temperature on elevation combined with an exponential dependence of precipitation on temperature. At the ice–ocean interface we use the Potsdam Ice-shelf Cavity mOdel (PICO)[63], which calculates melt patterns underneath the ice shelves for given ocean conditions[64]. Ocean temperature anomalies are computed from ice-core derived surface-temperature anomalies convolved with a response function to produce a damped and delayed response[65]. The calving front can freely evolve with calving parameterized to be dependent on principal strain rates at the ice-shelf front[66]. Basal sliding is parameterized using an iterative optimization scheme[67] modified for the till-friction angle, mimicking the distribution of marine sediment and bedrock, such that the mismatch to modern surface elevation observations is minimized.

Sea-level change drives grounding-line migration through the flotation criterion, which determines grounding-line position[68]. We prescribe sea-level changes by considering the height of the sea surface and the height of the sea floor separately. Unless otherwise stated, we use global mean sea-surface heights prescribed by the ICE-6G GIA model[69]. According to this model, mean sea-surface height has risen by about 100 m since 14.5 kyr BP. Alternative sea-surface height records were considered as part of the sensitivity analysis discussed below.

Changes to the height of the sea floor and bed topography are modelled using an approach that reflects the deformation of an elastic plate overlying a viscous half-space. Calculations are carried out using the computationally efficient Fast Fourier Transform to solve the biharmonic differential equation for vertical displacement in response to ice-load change[70]. This approach can also be used to calculate vertical displacement in response to spatially varying water-load changes (more details below). A key advantage this approach has over traditional Elastic Lithosphere Relaxing Asthenosphere (ELRA) models is that the response time of the sea floor is not considered a constant, but depends on the wavelength of the ice-load perturbation. This formulation closely approximates the approach used within many GIA models[70]. Given that our ice-sheet model is not coupled to a GIA model, we are unable to prescribe self-consistent water-load changes or account for feedbacks associated with post-glacial changes to the rotational state of the Earth[71]. The effect of neglecting these processes is discussed below in the section on sea-level forcing.

Bed-elevation adjustment. With a resolution of 15 km and uncertain bed elevation, basal conditions and climate forcings, matching the present-day grounding-line position in the Weddell Sea required raising the ice-sheet bed in one key location (Bungenstock Ice Rise) to compensate for topographic information lost during remapping.

The present-day elevations of the sea bed and ice-sheet bed are regionally highly uncertain[29,72]. Furthermore, when remapping observed bed elevations (Bedmap2; ref. [29]) from a relatively fine spatial grid (1 km) to the spatial resolution of our simulations (15 km), we lose bed-elevation information in key places. Remapping introduces inherent uncertainty into any low-resolution ice-sheet modelling study, but it is particularly important for the process of ice-rise regrounding that we highlight. For example, at present-day ice rises the remapping of the bed-elevation data reduces the apparent peak bed elevation by 36–135 m, while at their steep flanks this difference can be a few hundred metres (Extended Data Fig. 4). We find that in our simulations, if we use bed topography remapped directly from the Bedmap2 compilation (using a first-order conservative technique[73]), the grounding line in the Weddell Sea sector does not re-advance across a 1,300m-deep trough and often remains near to its Holocene minimum position, far inland of its present-day location, until the end of simulations. This is unrealistic.

We have experimented with various approaches to dealing with the uncertainty introduced by remapping bed topography to lower spatial resolutions. These include adopting the maximum Bedmap2 value in each model grid cell, either in the regions of individual ice rises or across the whole ice sheet. We also experimented with a sub-grid pinning point scheme, dependent upon the thickness of the water column underneath the ice shelf within some uncertainty range[74] and with a simpler uniform adjustment in the region of individual ice rises. Which approach we take affects the timing and magnitude of grounding-line retreat and re-advance. Without a clear motivation to adopt a more complex approach, we made the minimum adjustment to the bed that allowed the grounding line to re-advance in the Weddell Sea sector: we uniformly raised the bed by 150 m in a 165 km by 180 km area centred on Bungenstock Ice Rise (BIR) only. This rather arbitrary choice is a major limitation of this model ensemble, which (along with other uncertainties associated with model resolution, forcings, parameters and physics; see below) prevents us from extracting information about the timing of grounding-line retreat and re-advance from our simulations.

The purpose of our model experiments is to explore the mechanisms that could have caused re-advance and what influences these mechanisms. It is beyond our scope to explore the range of options to compensate for basal topographic remapping errors, but our work highlights that, at least for studying ice-rise regrounding, resolving this issue will be required if we are to make quantitative predictions of millennial-scale ice-sheet behaviour.

Model ensemble and the reference simulation. We performed an ensemble of simulations, each spanning 205 kyr BP to the present, in which uncertain parameters were systematically varied and the results were compared with palaeo-ice-sheet datasets and present-day observations[75,76]. The full results of the ensemble represent a likely range of Antarctic ice-sheet chronologies and will be presented elsewhere. Here we focus on the possible extent and triggers of large-scale grounding-line re-advance during the Holocene, and so discuss in detail only those mechanisms that are relevant to this process. We choose one of the ensemble members to act as a reference simulation to demonstrate aspects of model behaviour. The reference simulation is chosen from many ensemble members that use parameters lying within physically plausible bounds (Extended Data Table 2) and which also achieve reasonable agreement with a commonly used ice-sheet grounding-line position reconstruction[2]. Although this grounding-line reconstruction does not include grounding-line re-advance during the Holocene, as discussed in the main text, many ensemble members—including our reference simulation—simulate the grounding line retreating substantially inland of its present-day position and subsequently re-advancing towards its present position. We express ice-mass changes as the above-flotation volume in units of global sea-level equivalent, assuming a constant ocean area of 3.61×10^{14} m^2 (ref. [77]).

The drivers of grounding-line re-advance. We performed three model experiments (separate from the full ensemble, above) in order to disentangle the causes of re-advance in the Weddell and Ross Sea sectors. We find that both uplift of the bed at the grounding line and buttressing caused by the formation of ice rises drive re-advance of the grounding line towards its present-day position in both the sectors (Extended Data Fig. 4). The first experiment ('No uplift'; Extended Data Fig. 4) is identical to the reference simulation except that uplift is halted after 10 kyr BP—that is, at approximately the time at which the grounding line in the reference simulation reaches its most retreated position in both sectors (Fig. 3). The grounding line in the Weddell Sea remains at its 10 kyr BP position for the remainder of the simulation. In the Ross Sea the grounding line retreats further into the interior of the ice sheet. This additional retreat can be prevented by buttressing, as demonstrated in the second experiment ('No uplift, grounding of ice rises'; Extended Data Fig. 4), where uplift is again halted at 10 kyr BP, but ice-rise formation is enforced by raising the seafloor in the locations of the Crary, Steershead, Henry and Korff ice rises and Doake Ice Rumples. In this simulation, further retreat in the Ross Sea is prevented, but re-advance still does not occur in either sector. We further test the relevance of buttressing via ice-rise formation in a third experiment ('Uplift, no grounding of ice rises'; Extended Data Fig. 4), in which uplift of the bed is allowed, but ice-rise formation is prevented by lowering the seafloor. In this simulation ice-shelf buttressing is reduced compared with the reference simulation. Consequently, the grounding line remains at its 10 kyr BP position in the Weddell Sea (Extended Data Fig. 4a) and relatively little re-advance occurs in the Ross Sea (Extended Data Fig. 4b). Hence we identify the grounding of HIR, as evident from our radar survey, as critical for grounding-line re-advance in the Weddell Sea in these simulations; meanwhile, in the Ross Sea, neither uplift in the grounding-line region nor buttressing resulting from ice-rise formation is alone sufficient to drive grounding-line re-advance to the present-day position.

Model sensitivity to forcings. Extended Data Fig. 6 plots selected results from our analysis of the sensitivity of the model to various forcings. The retreat of the grounding line inland of its present-day location and its subsequent re-advance is a common behaviour in the model; however, its minimum extent during the Holocene, and how fast and how far it re-advances, are all sensitive to forcings.

Given that sea-level forcing is highly relevant for deglaciation, we compared the responses to four different eustatic sea-level reconstructions (Extended Data Fig. 6a). In our reference simulation, we use the sea-level curve from the ICE-6G model[69]. Refs [78,79] provide similar sea-level reconstructions and hence similar model results, with the strongest changes after around 15 kyr BP. We also used the SPECMAP time series[80] (as used in the SeaRISE intercomparison[77]); the results show a delayed LGM sea-level lowstand and a delayed sea-level rise to Holocene conditions, and hence the modelled ice sheet exhibits a later retreat and re-advance (Extended Data Fig. 6).

In order to mimic the first-order effects of GIA coupling[81] (including rotational feedback and self-gravitational effects), we experimented with scaling the time series of sea-level forcing by factors of 0.9 and 0.8 (initiated at 35 kyr BP; Extended Data Fig. 6b). We do not attempt to prescribe spatially varying sea-level forcing, but comparison with independent GIA model output[82] suggests that neglect of rotational feedback and self-gravitation of the ocean may result in local errors in sea-level forcing of the order of 15–20 m (this range reflects the likely error associated with prescribing sea-surface height; deformation of the seabed is self-consistently modelled within PISM). Scaling the uniform sea-level forcing by a factor of 0.9 causes the lowstand to be less pronounced at the LGM (approximately 10 m higher), in comparison with the reference simulation. This affects the LGM grounding-line position, particularly in the Ross Sea, which in turn affects the retreat and re-advance of the grounding line, because the depression of the bed depends sensitively on the ice-sheet's LGM extent. Scaling by 0.8 may be unrealistic (on the basis of comparison with GIA model output generated using an independent ice-sheet history[82]; data not shown), and interestingly, we note that retreat behind the present-day grounding-line position is not reproduced in this scenario (Extended Data Fig. 6b). We also experiment with a sea-level forcing that is identical to that used in the reference simulation (ICE-6G model[69]) except that the curve has been uniformly shifted 2 kyr earlier. The result is that the grounding line responds with an earlier retreat. This response emphasizes the key role of the sea-level forcing in triggering large-scale grounding-line retreat.

Sea-level changes also affect the load of the ocean on the sea bed. This triggers bed deformation, which will affect grounding-line migration. By default, this second-order effect is not accounted for in PISM. However, we carried out exploratory simulations that do account for it (data not shown), and find that when grounding-line retreat is accompanied by an increase in eustatic sea level, the additional ocean load partly counteracts the unloading associated with grounding-line retreat. Accordingly, the grounding line retreats further inland than in the reference simulation. On the other hand, sea-bed uplift following grounding-line retreat reduces the water load in marine sectors; this further amplifies uplift, which supports grounding-line advance. These interesting second-order effects do not qualitatively affect model behaviour, but they do influence the magnitude of grounding-line retreat and re-advance through their influence on LGM extent in both the Weddell and Ross sectors.

For surface-temperature forcing, our reference simulation uses a reconstruction based on data from the WAIS divide ice core (WDC)[60]. The results are similar when an alternative reconstruction from the EPICA Dome C ice core (EDC)[83] is used (Extended Data Fig. 6c). However, the grounding line responds to the slightly warmer LGM conditions in the EDC case with less LGM advance and hence a less severe retreat in the Ross Sea sector. For comparison, we also force one simulation with a temperature record pertaining to the start of the Last Interglacial Period (from the EDC core), in which an earlier and stronger warming leads to an earlier and stronger grounding-line retreat, particularly in the Ross Sea sector.

Accumulation in the reference simulation is coupled to changes in surface temperature by imposing a 2% precipitation change for each degree of variation from present-day temperatures (Extended Data Fig. 6d; violet curves) resulting from climatic changes (constrained by ice-core data), and a 43% precipitation change per km of surface-elevation change. We experimented with two alternative time-dependent accumulation forcings and two constant accumulation scenarios. Using either a scaling of 5% per degree of WDC-temperature change or an independent WDC-derived accumulation reconstruction[84] leads to lower mean accumulation and a less advanced LGM grounding-line position (Extended Data Fig. 6d). The less advanced LGM grounding line almost eliminates grounding-line retreat inland of its present position and re-advance, particularly in the Weddell Sea. When accumulation is kept constant at LGM conditions (2% per degree scaling of the EDC temperature at 25 kyr BP; Extended Data Fig. 6d), which correspond to 18% lower accumulation than today, the grounding line retreats inland of its present-day location in both sectors, but only partially re-advances in the Ross Sea and does not re-advance in the Weddell Sea. When accumulation is kept constant at present-day values (Extended Data Fig. 6d), grounding-line retreat starts earlier than in the reference simulation, particularly in the Ross Sea. In both sectors the grounding line retreats and re-advances in a similar way to the reference simulation, but with different timings: in the Weddell Sea the grounding line re-advances several thousand years earlier than in the reference simulations, while in the Ross Sea re-advance is delayed in comparison with the reference simulation.

Model sensitivity to parameters. Next we used selected members of the ice-sheet model ensemble to demonstrate the sensitivity of the model to various parameter values. Analysis of the full model ensemble, including a systematic validation of the full range of parameter combinations against present-day conditions and reconstructions of past conditions[27,76], will be presented elsewhere. Here we present the impact of single parameter perturbations. In general, we find that retreat of the grounding line inland of its present-day location and subsequent re-advance occurs over a wide range of parameter choices, but the Holocene minimum extent, and how fast and how far the grounding line re-advances, are sensitive to these choices.

Mantle viscosity affects model behaviour because it defines the rate and pattern of the deformation of the ice-sheet bed and sea floor. Our reference simulation uses a mantle viscosity of 5×10^{20} Pa s. The ensemble also covers a value considered typical for pan-Antarctic model simulations and often used as the default value in other PISM simulations (1×10^{21} Pa s; Extended Data Fig. 7a). We selected the lower value for our reference simulation to account for the weaker mantle beneath the WAIS[85]. An even lower viscosity (roughly 1×10^{20} Pa s; Extended Data Fig. 7a) has also been tested. In the lowest viscosity case, retreat of the grounding line inland of the present-day position is prevented as the bed responds too quickly to ice unloading. We find the fastest grounding-line retreat rates for higher viscosities. The most inland position reached by the grounding line is similar in each case, except the lowest viscosity case, and re-advance occurs earlier for lower mantle viscosity. In summary, we find that grounding-line retreat and re-advance occurs in a plausible but confined range of mantle viscosity values.

Flexural rigidity is associated with the thickness of the elastic lithosphere and has an influence on the horizontal extent to which bed deformation responds to changes in load. Previous studies based on gravity modelling suggest appropriate values for our study with a focus on West Antarctica lying within the range 5×10^{23} to 5×10^{24} N m (refs [86,87]). Our reference simulation marks the upper end of this range (Extended Data Fig. 7a). For lower values, 1×10^{24} to 5×10^{23} N m, we find grounding-line retreat beyond its present-day location and re-advance as in the reference simulation. However, maximum retreat is delayed in the Ross Sea sector, so re-advance of the grounding line does not reach its present-day location in that sector.

Enhancement factors are used in ice modelling to account for anisotropy and other unresolved rheological properties and enter the constitutive law. PISM uses one enhancement factor for the shallow-shelf approximation (SSA) component of the stress balance, and a second enhancement factor for the shallow-ice approximation (SIA) component. Increasing the SSA enhancement factor (Extended Data Fig. 7b) and/or decreasing the SIA enhancement factor (Extended Data Fig. 7c) produces a less advanced LGM grounding-line position. This is because larger values of the SSA enhancement factor produce faster ice streams and thinner ice shelves, and smaller values of the SIA enhancement factor produce thicker grounded ice. For a less advanced LGM grounding line, retreat begins earlier and progresses more slowly, and does not reach as far inland before retreat is halted.

PISM uses a generalized sliding parameterization formulated as a power law[59], spanning a range from plastic Coulomb sliding (with sliding exponent $q = 0$) to sliding in which till strength is linearly related to sliding velocity ($q = 1$). In the reference simulation we use $q = 0.75$ (Extended Data Fig. 7d). In the linear case ($q = 1$), the LGM grounding line is less advanced and retreat starts earlier (Extended Data Fig. 7d). For smaller values of q, retreat occurs generally later in the Weddell Sea and retreat in the Ross Sea is less pronounced.

Two other parameters associated with the sliding parameterization are the decay rate of till water and the effective overburden pressure[59]. Within the range explored by the ensemble, both parameters have only a moderate effect on the LGM extent of the grounding line and the timing of retreat, and do not affect whether or not the grounding line retreats inland of its present-day location and re-advances (Extended Data Fig. 7e).

A final sliding-related parameter is the till friction angle, which varies spatially and for our reference simulation is optimized[67] to minimize the mismatch between modelled and observed surface elevation, but is constrained to be larger than 2°. Reducing the minimum value to 1° leads to a smaller LGM extent and hence a slower retreat and larger minimum extent (preventing retreat past the present-day grounding-line position in the Weddell Sea) (Extended Data Fig. 7f). Instead of optimizing the till friction angle using observed surface elevations, it can also be defined as a linear piecewise function of bed topography, with 2° used in areas below -500 m (this is the default approach in PISM)[59]. This also reduces the LGM extent and, in the Ross Sea, reduces the retreat of the grounding line inland of its present-day extent.

Ocean forcing in our simulations is modelled with PICO[63]. PICO uses parameters for overturning strength and heat exchange. Modification of the parameter values affects the LGM extent of the grounding line and hence the rate and timing of retreat (Extended Data Fig. 7g). However, grounding-line retreat and re-advance are produced as robust features for extreme parameter values, even if melting is omitted or prescribed as a constant at present-day values.

Calving is parameterized as eigencalving (dependent on strain rates)[66]. A parameter K is the constant of proportionality between the calving rate and the horizontal spreading rate of ice shelves (Extended Data Fig. 7h). K is assumed to be constant and uniform. Our reference simulation uses $K = 1 \times 10^{17}$ m s. The LGM grounding-line position is less advanced for smaller eigencalving values, and grounding-line retreat less pronounced, probably because of additional ice-shelf buttressing resulting from less calving.

Resolution dependence. Our simulations, in common with all millennial-timescale ice-sheet simulations, suffer from major limitations related to the maximum practical spatial resolution that they can use. Just like the model parameters considered in the previous section, the spatial resolution can be treated as a quantity that affects the results of the simulations and should be investigated. This is particularly true in our study, as ice-shelf grounding on bathymetric highs with relatively small horizontal dimensions has proven to be so important for the large-scale evolution of the ice sheet.

A sensitivity analysis aimed at examining the sensitivity of this behaviour to resolution (analogous to the exercise described above) is highly limited by computational resources. For example, doubling the spatial resolution incurs at least a tenfold increase in computational cost. Ensembles with systematically varied parameters of simulations that span the full spin-up over two glacial cycles (205 kyr) are at present possible only with a spatial resolution of 15 km.

Shorter simulations (that cover only the past 20 kyr) are possible using a resolution of up to 7 km, if they are initiated at 20 kyr bp by remapping the spun-up state of a 15-km-resolution simulation. (Unfortunately, this remapping means that, despite the higher resolution, the bed topography is no better resolved with respect to observations[29] than the 15-km-resolution simulations.) Higher-resolution simulations generally reproduce the pattern of grounding-line retreat and re-advance, but the increase in resolution strongly affects the timing and magnitude of changes (Extended Data Fig. 8). Owing to the influence of resolution on other model parameters, a full ensemble analysis at higher resolution would be required to fully characterize the resolution dependence of our simulations. Furthermore, these simulations would need to use the higher resolution throughout the 205-kyr spin-up period in order to benefit from better-resolved bed topography. This is unfeasible with currently available computing resources.

Geophysical and terrestrial evidence consistent with re-advance. Previous geophysical and terrestrial observations are consistent with our proposed sequence of retreat and re-advance, but do not yet provide a coherent pattern of retreat and re-advance. Their spatial coverage is presently insufficient to reveal the full complexity of Holocene retreat and re-advance. For the Weddell Sea, ref. [53] presented evidence that Korff Ice Rise (KIR; Fig. 1) has been in a steady configuration since around 2.5 kyr bp. However, before that time KIR could have undergone substantial flow disturbance—including near-complete ungrounding and regrounding (as in our reference simulation; Supplementary Video 1)—if subsequent steady ice flow has had enough time to remove englacial evidence of such a flow disturbance. See ref. [53] for details of this interpretation. Radar data from BIR (Fig. 1) suggest a reorganization in flow as early as 4 kyr bp (ref. [10]), while regional uplift rates suggest that BIR may have been ungrounded between 4 kyr bp and 2 kyr bp (ref. [5]). In the Ellsworth[88] and Pensacola[89,90] Mountains, geological exposure-age dating techniques constrain the thinning of the ice during the Holocene. These studies cannot provide evidence for re-thickening, which could be associated with re-advance, but the results cannot rule out the possibility of lowering of the ice-sheet surface below its present-day height and subsequent re-thickening within the last 4 kyr or so[91]. Ref. [92] noted that radar-derived basal topography upstream of a subglacial basin beneath the Institute and Möller ice streams suggests a former grounding-line position more than 100 km upstream of today's grounding line, although these authors did not suggest that this was a Holocene grounding-line position.

Similarly, in the Ross Sea exposure-age dating in the Trans-Antarctic Mountains (see, for example, refs [3,4,40,93]) may be consistent with our conclusions, but cannot confirm or rule-out re-advance. Geophysical observations have hinted at recent re-advance. Borehole temperatures have been used to date the grounding and formation of Crary Ice Rise (CIR; Fig. 1b) to 1.5–1.0 kyr bp (ref. [57]) and ice-penetrating radar surveys of Kamb Ice Stream indicate that the grounding line was upstream of its present location during the past few centuries[9]. However, it is unclear whether the latter observation is evidence for a long-term large-scale re-advance, or for relatively-small-scale grounding-line fluctuations.

In both sectors, it is unclear whether these varied observations from diverse glacial environments (outlet glaciers, ice streams, ice rises and nunataks) paint a consistent picture of the timing of retreat and re-advance. Our work does not provide any detailed timing constraints; the timing of simulated grounding-line migration depends on uncertain bed topography and model parameters, and further work is needed to extract timing information from our radiocarbon and radar observations. We leave to future work the important task of unravelling a retreat–readvance chronology consistent with all observations.

Code availability. The PISM code used in this study can be obtained from https://doi.org/10.5281/zenodo.1199066. Results and plotting scripts are available from https://doi.org/10.5880/PIK.2018.008. Scripts for processing and plotting radar data are also available on request.

Data availability. Ice-penetrating radar data can be obtained from the UK Polar Data Centre at http://doi.org/99d. A simple MATLAB script for viewing the raw radar data is also provided at this link. The radiocarbon data supporting the findings of this study are available in Extended Data Table 1.

33. Lipps, J. H., Ronan, T. DeLaca, T. Life below the Ross ice shelf. *Antarct. Sci*. **203**, 447–449 (1979).
34. Coenen, J. J. *Inferring West Antarctic Subglacial Basin History and Ice Stream Processes Using Siliceous Microfossils*. MSc Thesis, Northern Illinois Univ. (2016).
35. Scherer, R. P. et al. Pleistocene collapse of the West Antarctic ice sheet. *Science* **281**, 82–85 (1998).
36. Abbott, M. B. & Stafford, T. W. Jr. Radiocarbon geochemistry of modern and ancient Arctic lake systems, Baffin Island, Canada. *Quat. Res*. **45**, 300–311 (1996).
37. Priscu, J. C. et al. A microbiologically clean strategy for access to the Whillans Ice Stream subglacial environment. *Antarct. Sci*. **25**, 637–647 (2013).
38. Rosenheim, B. E. et al. Improving Antarctic sediment 14 C dating using ramped pyrolysis: an example from the Hugo Island trough. *Radiocarbon* **55**, 115–126 (2013).
39. Clark, P. U. et al. The last glacial maximum. *Science* **325**, 710–714 (2009).
40. Anderson, J. B. et al. Ross Sea paleo-ice sheet drainage and deglacial history during and since the LGM. *Quat. Sci. Rev*. **100**, 31–54 (2014).
41. Andrews, J. T. et al. Problems and possible solutions concerning radiocarbon dating of surface marine sediments, Ross Sea, Antarctica. *Quat. Res*. **52**, 206–216 (1999).
42. Licht, K. J. & Andrews, J. T. The ^{14}C record of Late Pleistocene ice advance and retreat in the central Ross Sea, Antarctica. *Arct. Antarct. Alp. Res*. **34**, 324–333 (2002).
43. McKay, R. et al. Retreat history of the Ross Ice Sheet (Shelf) since the Last Glacial Maximum from deep-basin sediment cores around Ross Island. *Palaeogeogr. Palaeoclimatol. Palaeoecol*. **260**, 245–261 (2008).
44. Martinerie, P. et al. Physical and climatic parameters which influence the air content in polar ice. *Earth Planet. Sci. Lett*. **112**, 1–13 (1992).
45. Federer, U. et al. Continuous flow analysis of total organic carbon in polar ice cores. *Environ. Sci. Technol*. **42**, 8039–8043 (2008).
46. Antony, R. et al. Organic carbon in Antarctic snow: spatial trends and possible sources. *Environ. Sci. Technol*. **45**, 9944–9950 (2011).
47. Joughin, I. et al. Melting and freezing beneath the Ross ice streams, Antarctica. *J. Glaciol*. **50**, 96–108 (2004).
48. Christner, B. C. et al. A microbial ecosystem beneath the West Antarctic ice sheet. *Nature* **512**, 310–313 (2014).
49. Tulaczyk, S., Kamb, B. & Engelhardt, H. F. Estimates of effective stress beneath a modern West Antarctic ice stream from till preconsolidation and void ratio. *Boreas* **30**, 101–114 (2001).
50. Christianson, K. et al. Basal conditions at the grounding zone of Whillans Ice Stream, West Antarctica, from ice-penetrating radar. *J. Geophys. Res. Earth Surf*. **121**, 1954–1983 (2016).
51. Hall, B. L. et al. Constant Holocene Southern-Ocean 14 C reservoir ages and ice-shelf flow rates. *Earth Planet. Sci. Lett*. **296**, 115–123 (2010).
52. Van Liefferinge, B. & Pattyn, F. Using ice-flow models to evaluate potential sites of million year-old ice in Antarctica. *Clim. Past* **9**, 2335 (2013).
53. Kingslake, J. et al. Ice-flow reorganization in West Antarctica 2.5 kyr ago dated using radar-derived englacial flow velocities. *Geophys. Res. Lett*. **43**, 9103–9112 (2016).
54. Scambos, T., Haran, T., Fahnestock, M., Painter, T. & Bohlander, J. MODIS-based Mosaic of Antarctica (MOA) data sets: continent-wide surface morphology and snow grain size. *Remote Sens. Environ*. **111**, 242–257 (2007).
55. Ely, J. et al. Insights on the formation of longitudinal surface structures on ice sheets from analysis of their spacing, spatial distribution, and relationship to ice thickness and flow. *J. Geophys. Res. Earth Surf*. **122**, 961–972 (2017).
56. Favier, L. & Pattyn, F. Antarctic ice rise formation, evolution, and stability. *Geophys. Res. Lett*. **42**, 4456–4463 (2015).
57. Bindschadler, R. A., Roberts, E. P. & Iken, A. Age of Crary Ice Rise, Antarctica, determined from temperature-depth profiles. *Ann. Glaciol*. **14**, 13–16 (1990).
58. Bueler, E. & Brown, J. Shallow shelf approximation as a "sliding law" in a thermomechanically coupled ice sheet model. *J. Geophys. Res. Earth Surf*. **114**, F03008 (2009).
59. The PISM authors. PISM, a Parallel Ice Sheet Model: user's manual (2017), based on development revision e9d2d1f8 (7 March 2017), http://www.pism-docs.org/wiki/lib/exe/fetch.php?media=pism_manual.pdf (2017).
60. Cuffey, K. M. et al. Deglacial temperature history of West Antarctica. *Proc. Natl Acad. Sci. USA* **113**, 14249–14254 (2016).
61. Ligtenberg, S. et al. Future surface mass balance of the Antarctic ice sheet and its influence on sea level change, simulated by a regional atmospheric climate model. *Clim. Dyn*. **41**, 867–884 (2013).
62. Frieler, K. et al. Consistent evidence of increasing Antarctic accumulation with warming. *Nat. Clim. Chang*. **5**, 348–352 (2015).
63. Reese, R. et al. Antarctic sub-shelf melt rates via PICO. *Cryosphere Discuss*. https://doi.org/10.5194/tc-2017-70 (2017).

64. Schmidtko, S. et al. Multidecadal warming of Antarctic waters. *Science* **346**, 1227–1231 (2014).
65. Li, C., von Storch, J. S. & Marotzke, J. Deep-ocean heat uptake and equilibrium climate response. *Clim. Dyn*. **40**, 1071–1086 (2013).
66. Levermann, A. et al. Kinematic first-order calving law implies potential for abrupt ice-shelf retreat. *Cryosphere* **6**, 273–286 (2012).
67. Pollard, D. & DeConto, R. A. simple inverse method for the distribution of basal sliding coefficients under ice sheets, applied to Antarctica. *Cryosphere* **6**, 953 (2012).
68. Feldmann, J. et al. Resolution-dependent performance of grounding line motion in a shallow model compared with a full-Stokes model according to the MISMIP3d intercomparison. *J. Glaciol*. **60**, 353–360 (2014).
69. Stuhne, G. & Peltier, W. Reconciling the ICE-6G_C reconstruction of glacial chronology with ice sheet dynamics: the cases of Greenland and Antarctica. *J. Geophys. Res. Earth Surf*. **120**, 1841–1865 (2015).
70. Bueler, E., Lingle, C. S. & Brown, J. Fast computation of a viscoelastic deformable Earth model for ice-sheet simulations. *Ann. Glaciol*. **46**, 97–105 (2007).
71. Milne, G., Mitrovica, J. X. & Davis, J. L. Near-field hydro-isostasy: the implementation of a revised sea-level equation. *Geophys. J. Int*. **139**, 464–482 (1999).
72. Pritchard, H. D. Bedgap: where next for Antarctic subglacial mapping? *Antarct. Sci*. **26**, 742–757 (2014).
73. Jones, P. W. First- and second-order conservative remapping schemes for grids in spherical coordinates. *Mon. Weath. Rev*. **127**, 2204–2210 (1999).
74. Pollard, D. & DeConto, R. M. Description of a hybrid ice sheet-shelf model, and application to Antarctica. *Geosci. Model Dev*. **5**, 1273–1295 (2012).
75. Briggs, R. D., Pollard, D. & Tarasov, L. A data-constrained large ensemble analysis of Antarctic evolution since the Eemian. *Quat. Sci. Rev*. **103**, 91–115 (2014).
76. Pollard, D., Chang, W., Haran, M., Applegate, P. & DeConto, R. Large ensemble modeling of the last deglacial retreat of the West Antarctic Ice Sheet: comparison of simple and advanced statistical techniques. *Geosci. Mod. Dev*. **9**, 1697–1723 (2016).
77. Bindschadler, R. A. et al. Ice-sheet model sensitivities to environmental forcing and their use in projecting future sea level (the SeaRISE project). *J. Glaciol*. **59**, 195–224 (2013).
78. Lambeck, K. et al. Sea level and global ice volumes from the Last Glacial Maximum to the Holocene. *Proc. Natl Acad. Sci. USA* **111**, 15296–15303 (2014).
79. Bintanja, R. & Van de Wal, R. North American ice-sheet dynamics and the onset of 100,000-year glacial cycles. *Nature* **454**, 869–872 (2008).
80. Imbrie, J. D. & McIntyre, A. SPECMAP time scale developed by Imbrie et al., 1984 based on normalized planktonic records (normalized O-18 vs time, specmap.017). *Pangaea* https://doi.org/10.1594/PANGAEA.441706 (2006).
81. Gomez, N., Pollard, D. & Mitrovica, J. X. A 3-D coupled ice sheet–sea level model applied to Antarctica through the last 40 ky. *Earth Planet. Sci. Lett*. **384**, 88–99 (2013).
82. Whitehouse, P. L., Bentley, M. J., Milne, G. A., King, M. A. & Thomas, I. D. A new glacial isostatic model for Antarctica: calibrated and tested using observations of relative sea-level change and present-day uplift rates. *Geophys. J. Int*. **190**, 1464–1482 (2012).
83. Jouzel, J. et al. Orbital and millennial Antarctic climate variability over the past 800,000 years. *Science* **317**, 793–796 (2007).
84. Fudge, T. et al. Variable relationship between accumulation and temperature in West Antarctica for the past 31,000 years. *Geophys. Res. Lett*. **43**, 3795–3803 (2016).
85. Hay, C. C. et al. Sea level fingerprints in a region of complex Earth structure: the case of WAIS. *J. Clim*. **30**, 1881–1892 (2017).
86. Ji, F. et al. Variations of the effective elastic thickness over the Ross Sea and Transantarctic Mountains and implications for their structure and tectonics. *Tectonophysics* **717**, 127–138 (2017).
87. Chen, B., Haeger, C., Kaban, M. K. & Petrunin, A. G. Variations of the effective elastic thickness reveal tectonic fragmentation of the Antarctic lithosphere. *Tectonophysics* https://doi.org/10.1016/j.tecto.2017.06.012 (2017).
88. Hein, A. S. et al. Mid-Holocene pulse of thinning in the Weddell Sea sector of the West Antarctic ice sheet. *Nat. Commun*. **7**, 12511 (2016).
89. Balco, G. et al. Cosmogenic-nuclide exposure ages from the Pensacola Mountains adjacent to the Foundation Ice Stream, Antarctica. *Am. J. Sci*. **316**, 542–577 (2016).
90. Bentley, M. J. et al. Deglacial history of the Pensacola Mountains, Antarctica from glacial geomorphology and cosmogenic nuclide surface exposure dating. *Quat. Sci. Rev*. **158**, 58–76 (2017).
91. Whitehouse, P. L. et al. Controls on Last Glacial Maximum ice extent in the Weddell Sea embayment, Antarctica. *J. Geophys. Res. Earth Surf*. **122**, 371–397 (2017).
92. Ross, N. et al. Steep reverse bed slope at the grounding line of the Weddell Sea sector in West Antarctica. *Nat. Geosci*. **5**, 393 (2012).
93. Todd, C., Stone, J., Conway, H., Hall, B. & Bromley, G. Late Quaternary evolution of Reedy Glacier, Antarctica. *Quat. Sci. Rev*. **29**, 1328–1341 (2010).
94. Jezek, K. C., Curlander, J. C., Carsey, F., Wales, C & Barry, R. RAMP AMM-1 SAR image mosaic of Antarctica, version 2. *National Snow and Ice Data Center* https://doi.org/10.5067/8AF4ZRPULS4H (2013).
95. Fürst, J. J. et al. The safety band of Antarctic ice shelves. *Nat. Clim. Chang*. **6**, 479–482 (2016).
96. WAIS Divide Project Members. Precise interpolar phasing of abrupt climate change during the last ice age. *Nature* **520**, 661–665 (2015).

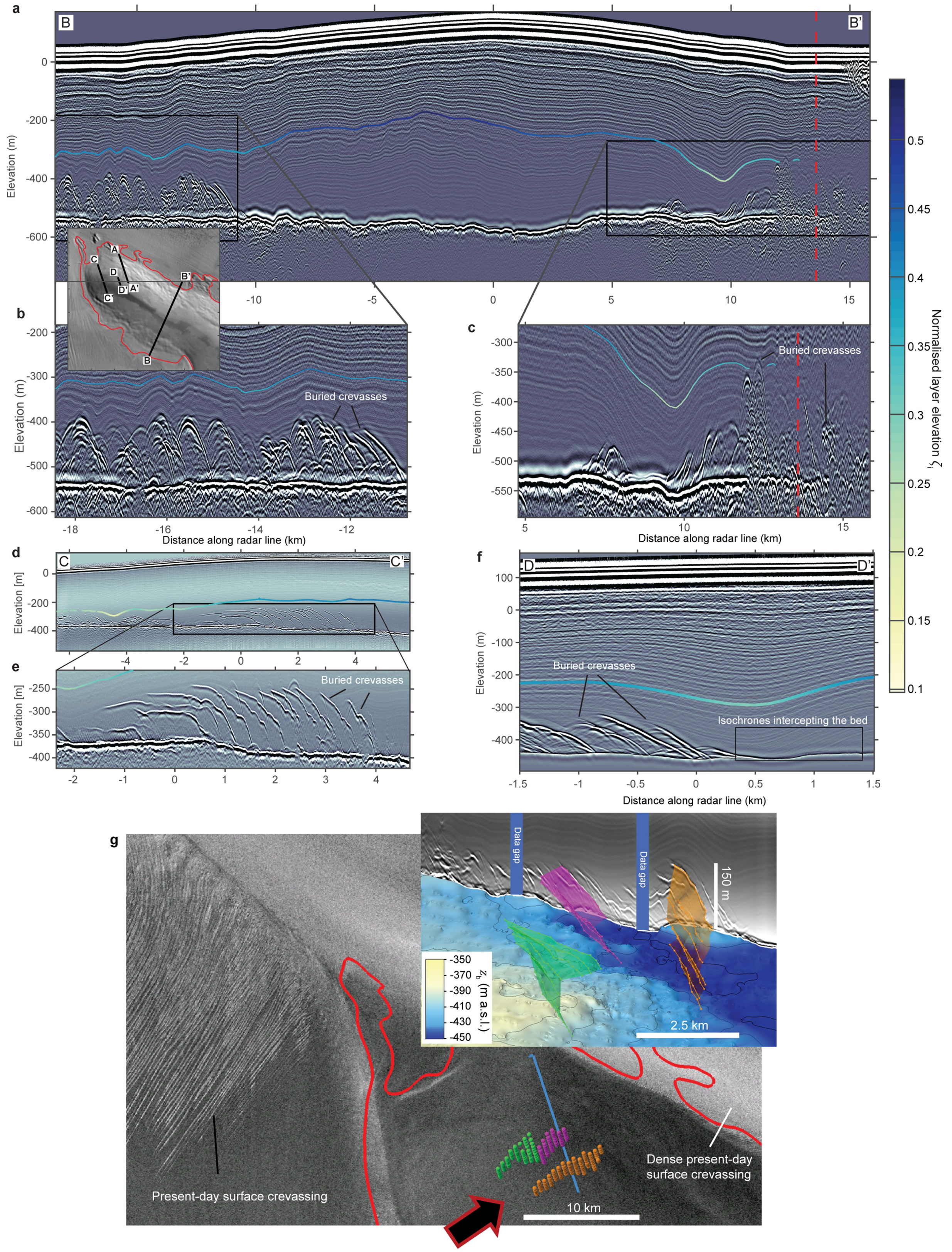

Extended Data Fig. 1 | Relic crevasses in Henry Ice Rise. a, Radargram, aligned perpendicular to the divide ridge (inset shows the location). One undulating isochrone is delineated with colours showing normalized elevation. **b**, **c**, Close-up views of the boxed regions indicated in **a**. In both close-up panels, diffractors (hyperbolic reflectors) are interpreted as expressions of relic crevasses (data are unmigrated). The red vertical dashed line is the present-day grounding line[31]. **d**–**f**, Radargrams aligned approximately perpendicular to northern relic crevasses (**d** and **e** show migrated data). In **c** (6 km $\leq x \leq$ 8 km) and **f** (0.3 km $\leq x \leq$ 1.4 km) isochrones intercepting the bed are evident. **g**, Three relic crevasses mapped across several radar lines over a Radarsat Antarctic Mapping Project (RAMP) image[94]. The inset is an oblique, three-dimensional view of the features over an interpolated surface, showing the bed elevation z_b (see Methods). Crevasse spacing in these areas ranges between approximately 200 m and 600 m. The arrow indicates the view direction of the oblique view.

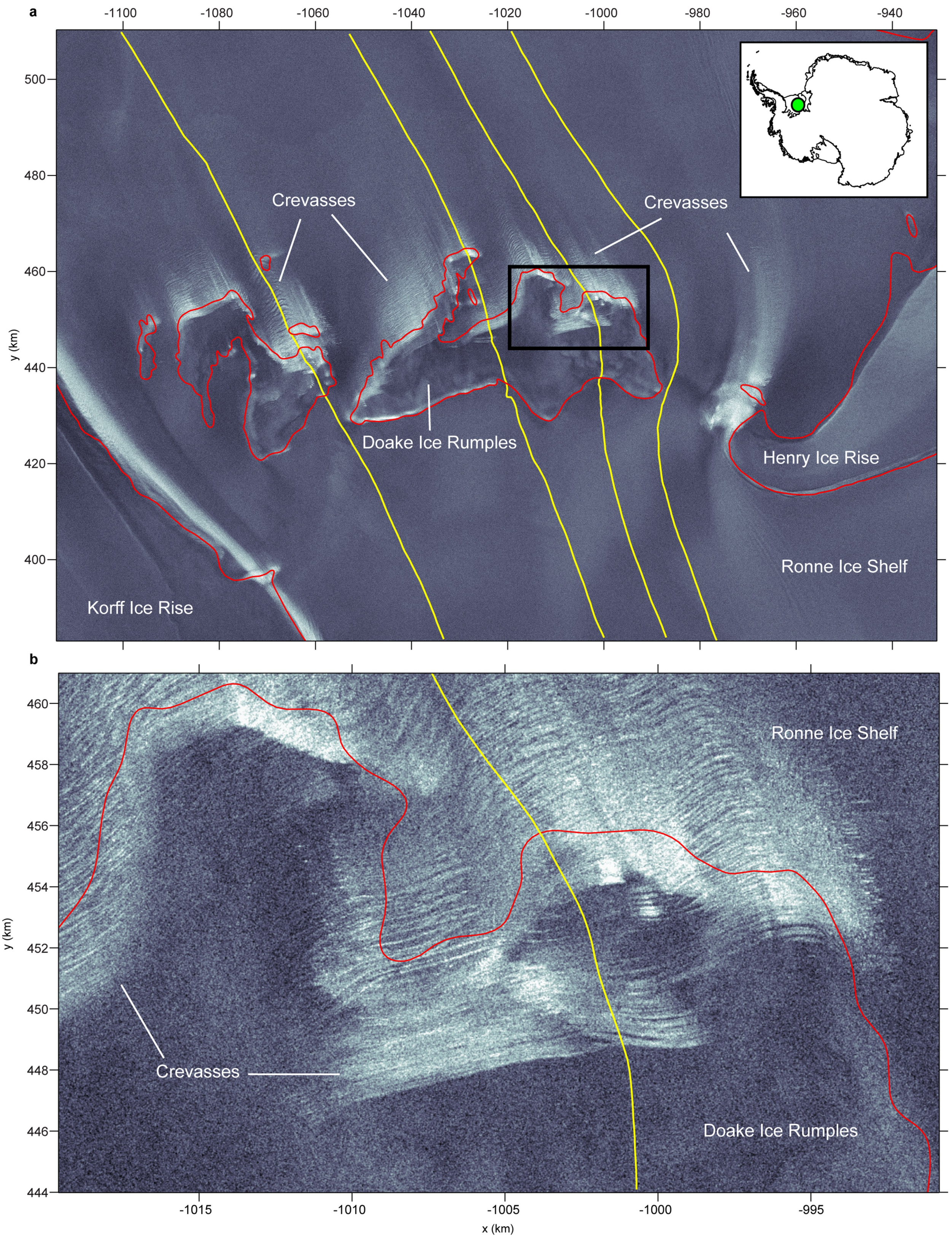

Extended Data Fig. 2 | Crevassing at Doake Ice Rumples. a, RAMP[94] image showing the surface expression of ice-shelf crevasses in synthetic aperture radar data. Light areas indicate high backscatter from (near-) surface reflectors, interpreted to be surface crevasses. Crevasses form over and immediately downstream of Doake Ice Rumples. We hypothesize that crevasses once formed in a similar manner over the topographic high beneath the northern tip of HIR. **b**, Close-up view of the crevasses (the black box in **a** shows the location), whose spacing (100–300 m), orientation (perpendicular to the flow of the ice shelf) and lateral extent (roughly 10 km) are similar to the steeply dipping reflectors discovered near the bed of the northern tip of HIR (for example, Extended Data Fig. 2g) in the region of a topographic high. Yellow curves are flow lines computed from satellite-derived surface velocities[30]. Flow is from bottom to top. Polar stereographic coordinates are in km. The present-day grounding line[31] is in red.

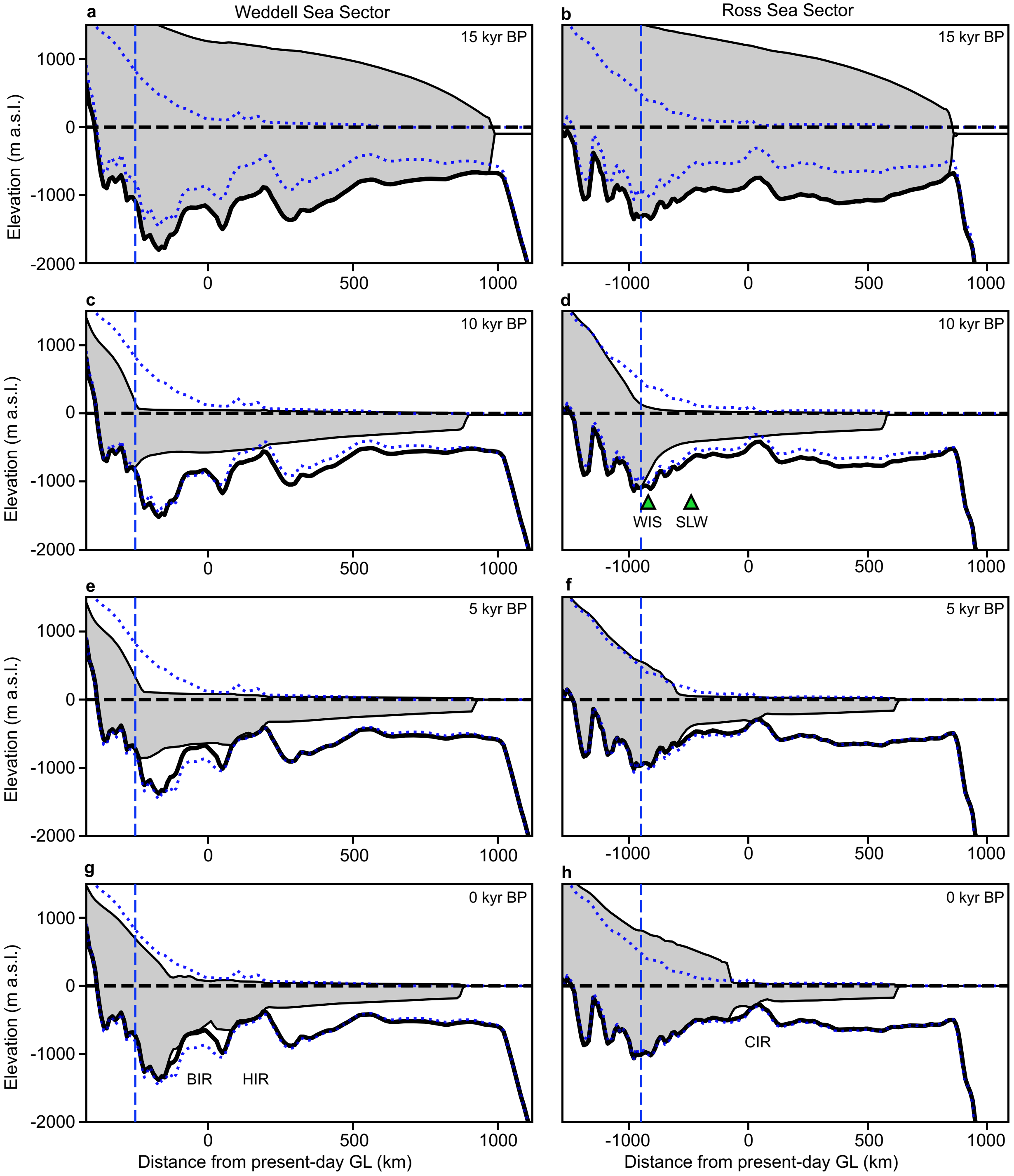

Extended Data Fig. 3 | Modelled grounding-line retreat and lithospheric rebound. Cross-sections along transects through the Weddell (left) and Ross (right) Sea sectors, at 5-kyr intervals (for transect locations, see Fig. 3). The horizontal axis shows the distance from the present-day grounding line. The vertical blue dashed line shows the position of maximum grounding-line retreat. **a**, **b**, 15 kyr BP, with the grounding line close to the continental shelf edge. **c**, **d**, 10 kyr BP, with the grounding line having retreated to approximately its minimum, most retreated location. **e**, **f**, 5 kyr BP, with both ice shelves grounded on sub-ice-shelf bathymetric highs owing to seafloor uplift. **g**, **h**, Present day, with the grounding line having re-advanced to roughly the present-day configuration in response to the grounding of the ice shelf and uplift at the grounding line. The Crary, Bungenstock and Henry ice rises (CIR, BIR and HIR) are labelled in **g** and **h**. The Whillans Ice Stream (WIS) and Subglacial Lake Whillans (SLW) sediment-core locations are labelled in **d**. Blue dotted lines show the observed present-day ice-sheet bed, ocean floor and ice surface[29], remapped on to the 15-km grid of the ice-sheet model.

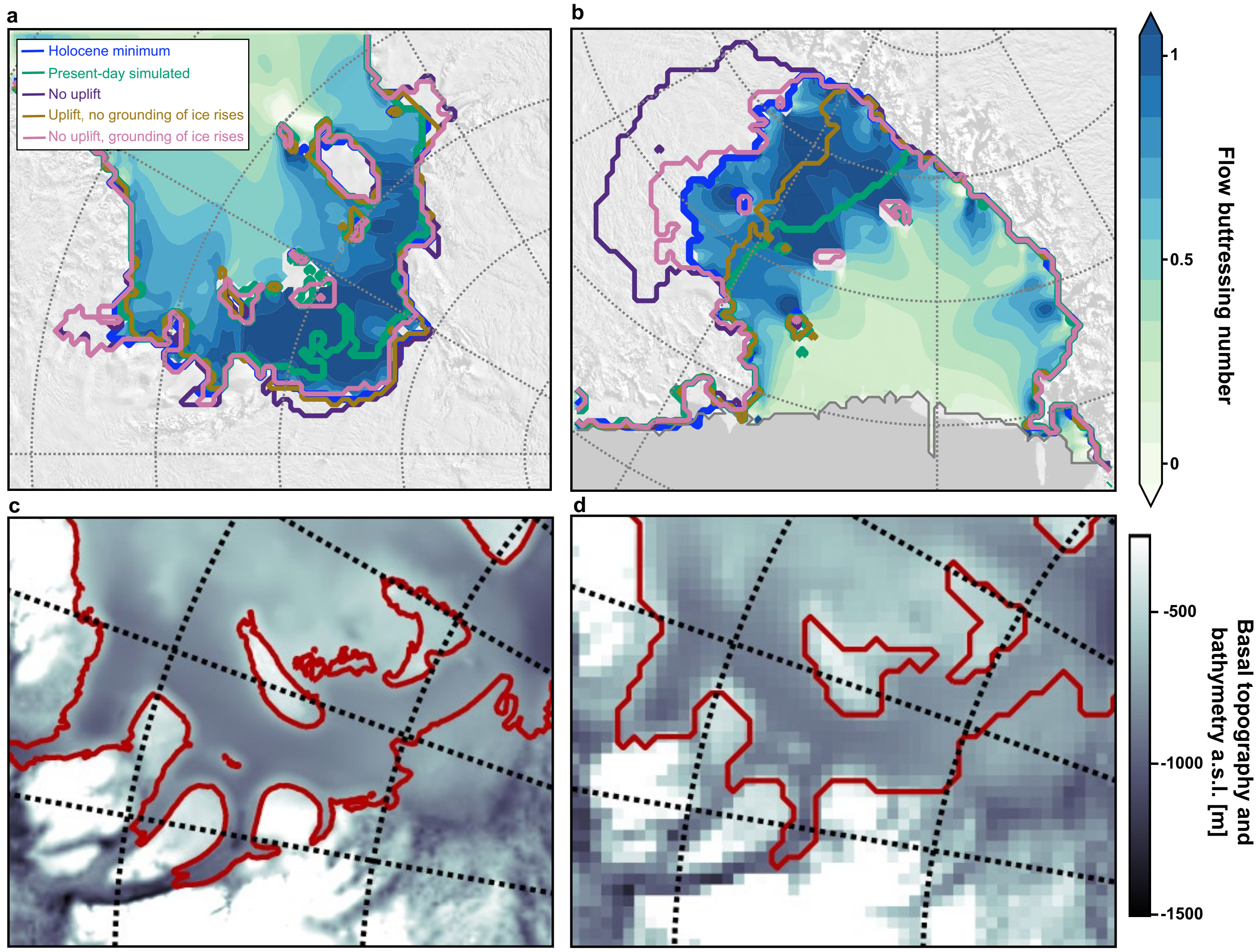

Extended Data Fig. 4 | Drivers of re-advance and the impact of bed re-mapping. a, **b**, Results from four simulations (the reference simulation, and three additional experiments) designed to examine the cause of re-advance in the Weddell Sea (**a**) and Ross Sea (**b**) sectors (Methods). The most inland grounding-line location in the reference simulation, at around 10 kyr BP, is in blue. The colour map shows the flow buttressing number[95] at 10 kyr BP in the 'No uplift, grounding of ice rises' experiment. The ice-front position is in grey. Background images over the grounded ice sheet are from MOA[32]. **c**, Basal topography and bathymetry in the Weddell Sea sector (with the grounding line in red) according to a 1-km-resolution dataset, constrained by geophysical observations (Bedmap 2; ref. [29]). **d**, Conservative remapping of these data to 15-km resolution. Remapping substantially lowers the apparent maximum bed elevations beneath ice rises in the Weddell Sea sector: 135 m at KIR, 112 m at HIR and 36 m at BIR.

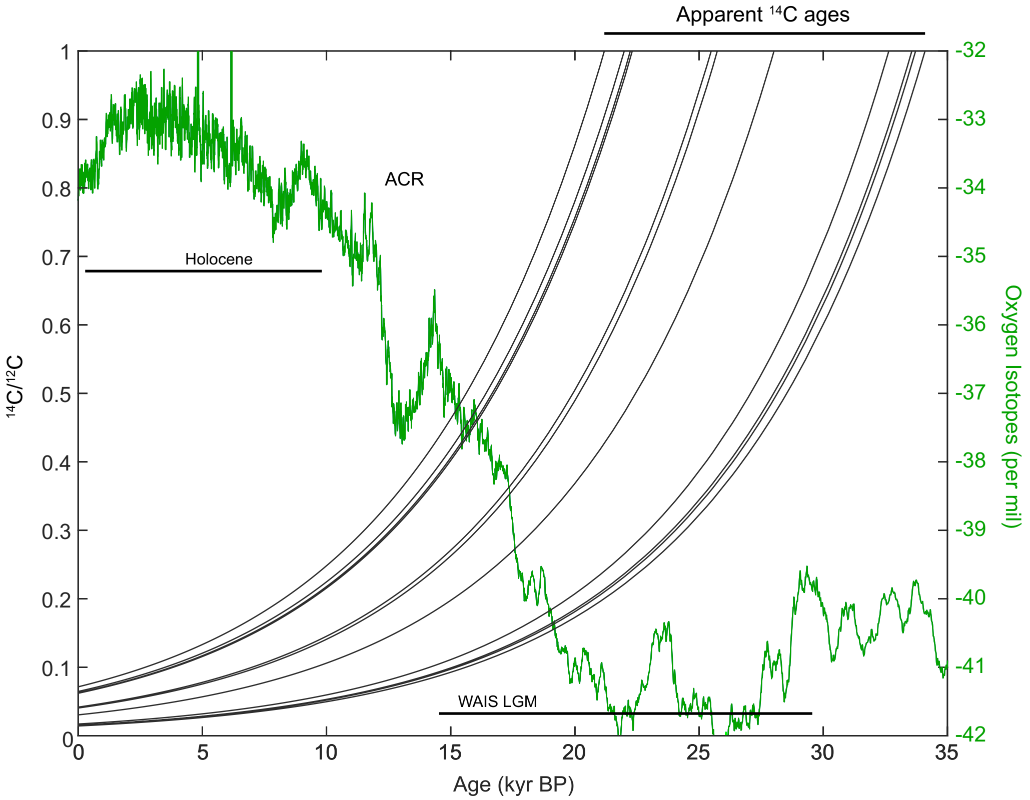

Extended Data Fig. 5 | True and apparent ages of radiocarbon. The 11 grey lines show exponential ^{14}C-decay curves connecting the ^{14}C/^{12}C ratios (scale on the left) measured on acid-insoluble inorganics (AIOs) from our subglacial sediment samples to the apparent radiocarbon ages calculated from these measurements. The latter calculation assumes that the initial ^{14}C/^{12}C ratios in AIOs were equal to the modern ratio in radiocarbon dating standards. As discussed in the text and Methods, organic matter in Antarctic glacigenic sediments frequently contains an admixture of old ^{14}C-dead material[41,42]. The record of oxygen isotopes in water ice from the WAIS Divide ice core (green line, with scale on the right) provides climatic context for the period between now and 35 kyr BP (ref. [96]). Three key climatic periods are labelled: WAIS LGM[39], Antarctic cold reversal (ACR) and Holocene.

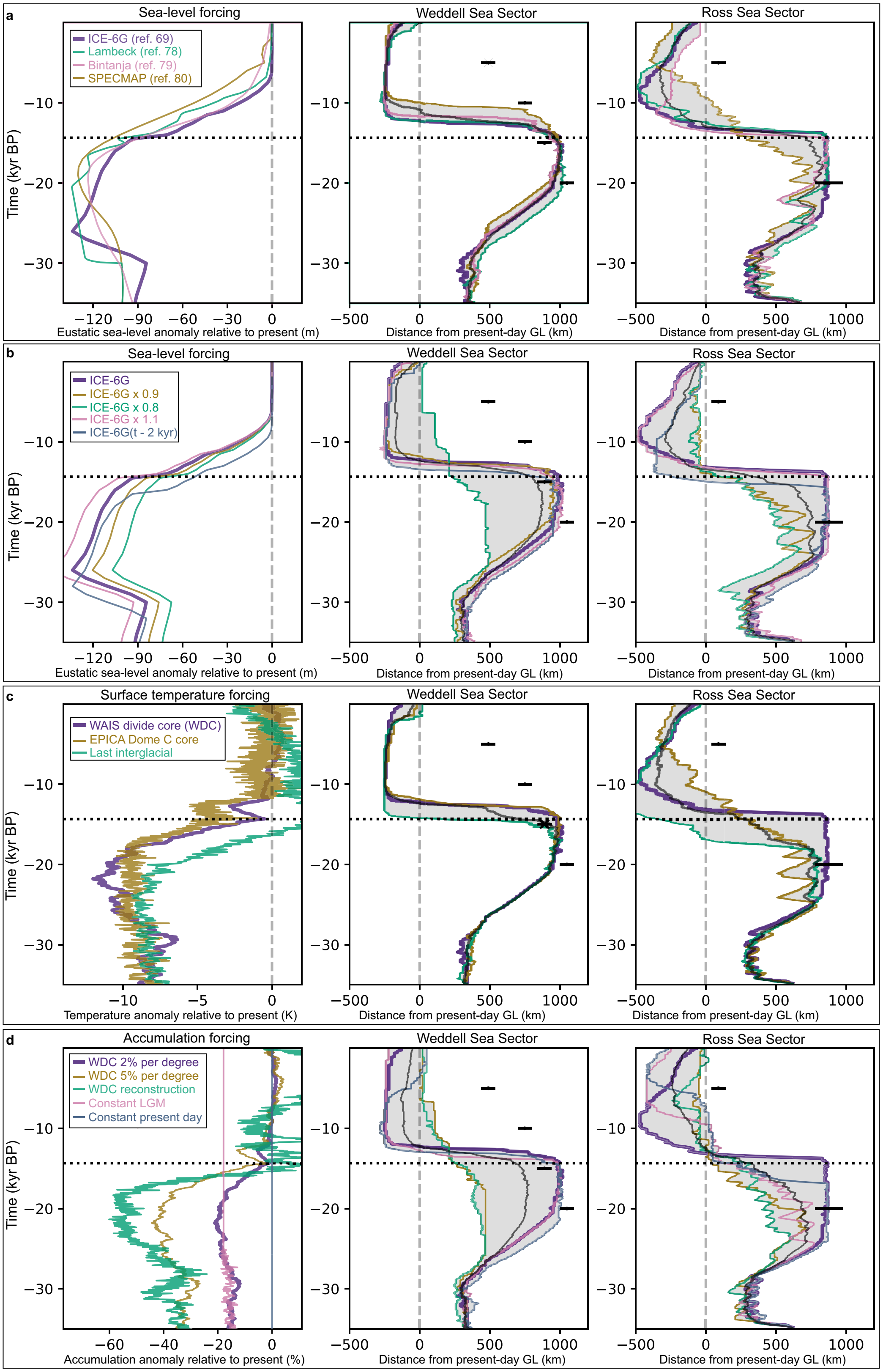

Extended Data Fig. 6 | See next page for caption.

Extended Data Fig. 6 | Model sensitivity to forcings. In the middle and right panels are time series of grounding-line position along transects, showing model sensitivity in the Weddell Sea (middle panels) and Ross Sea (right panels) sectors to: **a**, different sea-level reconstructions[69,78–80]; **b**, different scalings of the sea-level forcing to mimic self-gravitational effects; **c**, different surface-temperature forcings; and **d**, different accumulation forcings. In the left panels are: **a**, four alternative sea-level reconstructions; **b**, three alternative scalings of the reference-simulation sea-level forcing and a version that has been uniformly shifted 2,000 years earlier; **c**, temperature reconstructions from two ice cores, WAIS Divide and EPICA Dome C (EDC), and a reconstruction from the Last Interglacial (from EDC data); and **d**, four alternative accumulation histories. The constant LGM accumulation uses the EPICA Dome C core[83] and a scaling of 2% per degree. Temperature and accumulation are expressed relative to the present day. Grounding-line positions are relative to the present-day position (vertical dashed line) along the transacts shown in Fig. 3. In all simulations, the grounding line is in its most advanced position, up to 1,000 km beyond its present-day position, before MWP1a (14.4 kyr BP; horizontal dotted line). During the Holocene the grounding line retreats up to 500 km upstream of its present location, and usually re-advances towards its present-day position. Grey shading indicates the spread of grounding-line responses, and grey curves show the mean of each sensitivity experiment. In each case the violet curve shows the reference simulation. Grounding-line positions (based on marine and terrestrial geological evidence) from the RAISED reconstruction with associated uncertainties are shown in black[2].

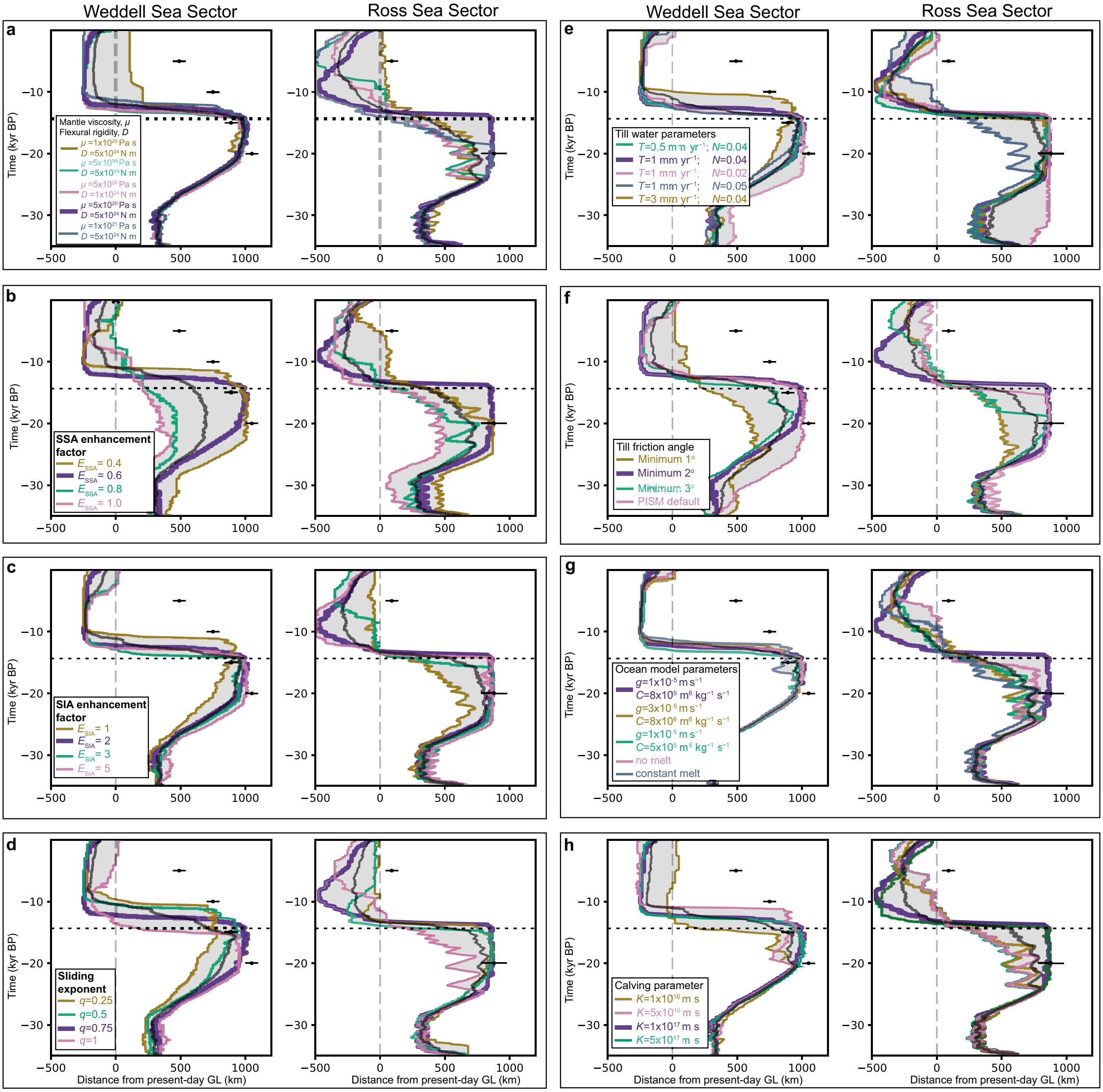

Extended Data Fig. 7 | Model sensitivity to parameters. Time series of grounding-line position along transects, showing model sensitivity in the Weddell and Ross Sea sectors to: **a**, mantle viscosity, μ, and the flexural rigidity of the lithosphere, D; **b**, **c**, enhancement factors E_{SSA} and E_{SIA}; **d**, the sliding-law exponent, q; **e**, the till water decay rate, T, and till effective pressure fraction, N; **f**, minimum till friction angle and the method used to derive the friction angle (see Methods); **g** PICO ocean model parameters for overturning strength, C, and heat exchange, g; and **h**, the dependence of calving rate on the ice-shelf spreading rate, K (Extended Data Table 2). In each panel, the violet curve shows the reference simulation. Grounding-line positions (based on marine and terrestrial geological evidence) from the RAISED reconstruction, with associated uncertainties, are shown in black[2].

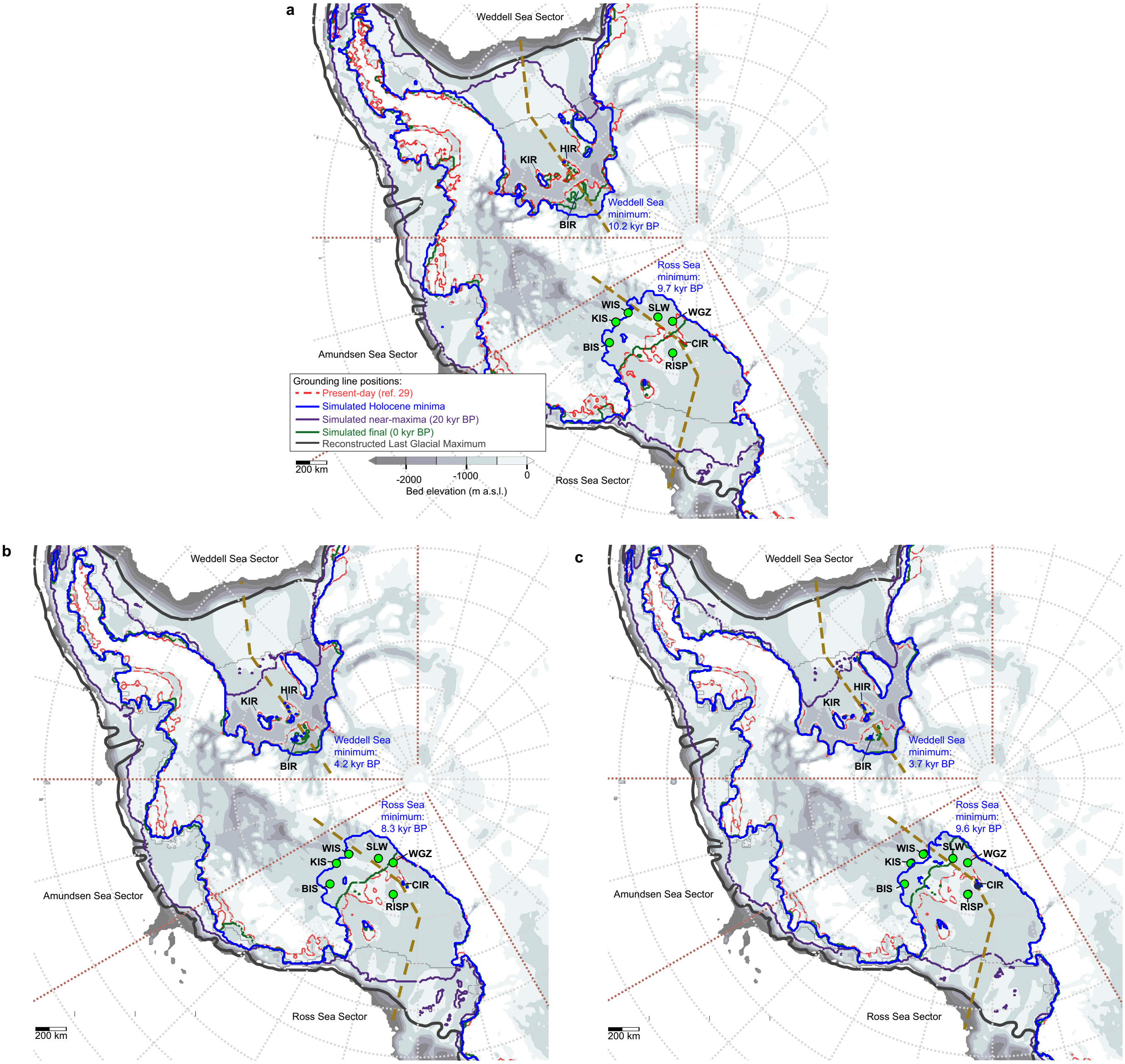

Extended Data Fig. 8 | Model sensitivity to spatial resolution. The results of three simulations using different grid resolutions: **a**, 15 km (reference simulation; identical to Fig. 3); **b**, 10 km; and **c**, 7 km. Owing to computational limitations, the two higher-resolution simulations cover only the past 20 kyr, so they lack a higher-resolution spin-up period. These higher-resolution simulations display similar Holocene retreat and re-advance driven by isostatic rebound to the reference simulation, but the LGM extent and grounding-line re-advance in the Weddell Sea are much less. A full exploration of the resolution dependence of the model requires using higher resolution during entire simulations for all ensemble members. This is limited at present by computing resources. Background shading shows basal topography and bathymetry[29].

Extended Data Table 1 | Results of radiocarbon and $\delta^{13}C$ analyses of subglacial sediments

K-Keck# Ua-Uppsala#	Sample Name	Fraction Modern	^{14}C Age (BP)	±	$\delta^{13}C$ ‰
K-166508	RISP Core 5 0-2 cm	0.0807	20,220	60	-28.2
K-166509	RISP Core 5 12-15 cm	0.0351	26,920	150	-27.0
K-166510	RISP Core 5 28.5-31.5 cm	0.0397	25,920	100	-25.7
K-166511	RISP Core 5 51-54 cm	0.0409	25,690	90	-26.2
K-166512	RISP Core 12 0-2 cm	0.1058	18,050	100	-27.8
K-166513	RISP Core 12 117-118cm	0.0604	22,550	70	-27.6
K-154083	WGZ-1 SS22 net bulk	0.0612	22,440	180	-27.3
K-160518	WGZ-1-MC1A-1-2cm	0.0809	20,205	50	-24.3
K-160516	WGZ-1-MC5A-3-5cm	0.0676	21,650	60	-24.1
K-160517	WGZ-1-MC5A-15-17cm	0.0424	25,400	80	-24.0
K-166502	WGZ-1 GC-4 9-11 cm	0.0240	29,950	220	-27.7
K-166503	WGZ-1 GC-4 36-38 cm	0.0213	30,930	240	-26.6
K-166504	WGZ-1 GC-4 45-47 cm	0.0541	23,440	120	-25.6
K-160514	WGZ-1-GC-4-13-16cm	0.0416	25,540	90	-25.9
K-160515	WGZ-1-GC-4-51-55cm	0.0562	23,120	70	-25.6
K-154080	WGZ-1 GP1-top SS-8	0.0580	22,870	260	-23.8
K-154081	WGZ-1 GP1-top SS-8	0.0576	22,930	190	-
K-154082	WGZ-1 GC-1 SS-7 86	0.0472	24,530	380	-25.3
K-160509	WGZ-1-GC-1-9-12cm	0.0433	25,220	100	-25.2
K-160510	WGZ-1-GC-1-38-43cm	0.0498	24,100	80	-23.9
K-160511	WGZ-1-GC-1-52-56cm	0.0437	25,140	140	-24.6
K-160512	WGZ-1-GC-1-65-68cm	0.0697	21,400	60	-24.3
K-160513	WGZ-1-GC-1-80-84cm	0.0441	25,070	90	-23.6
Ua-51811	WGZ-1, GC1, SS-7, 86 cm	-	28,687	161	-24'9
K-160521	SLW-PEC-1-34-35cm	0.0648	21,990	70	-24.6
K-154084	SLW-1 MC1B 0-8 bulk	0.0306	28,020	230	-24.9
Ua-51810	SLW-1, MC1B, 30-31 cm	-	29,378	180	-25,1
K-166505	UpB 89-4-50-53 cm	0.0406	25,740	100	-25.4
K-166506	UpB 89-7-50 cm	0.0419	25,490	90	-25.6
K-160519	UpB-88-89-SampleB2	0.0627	22,240	60	-26.1
K-160520	UpB-91-92-12-22-91-TV	0.0715	21,190	70	-25.4
K-166507	UpB 95-3-1-1	0.0621	22,320	70	-
K-166499	KIS 96-12-1-2-2-2 top 10cm	0.0150	33,720	230	-26.8
K-166501	KIS 96-7-1-3	0.0143	34,100	240	-26.7
K-166500	KIS 00-5-1-1C	0.0153	33,570	230	-26.7
K-166498	BIS 98-2-2-3c 60-70cm	0.0172	32,640	210	-26.5
K-154085	WGZ modern amphipod1	0.8738	1,085	20	-
K-154086	WGZ modern amphipod2	0.8746	1,075	15	-
K-154087	WGZ modern amphipod3	0.8669	1,145	15	-

Carbon-isotope results, including the fraction of modern carbon, calculated age, analytical error and independently measured $\delta^{13}C$ value. A low fraction of modern carbon relative to dominant ancient (radiocarbon-dead) carbon skews apparent ages older than the actual age of the marine connection discussed here. The light $\delta^{13}C$ results also point to a substantial source of old carbon. UpB is the upstream portion of the WIS.

Extended Data Table 2 | Key model parameters, with modelled retreat and re-advance

Parameter [Unit], symbol	Reference	Range	Relevance for LGM extent, overshoot of the present-day GL position during retreat and re-advance of the GL
Mantle viscosity [Pa s], μ	$5\text{x}10^{20}$	10^{20}-10^{21}	more overshoot retreat for higher values but delayed re-advance
Flexural rigidity [N m], D	$5\text{x}10^{24}$	5×10^{23}-5×10^{24}	smaller values delay retreat and re-advance
SSA enhancement [ ], E_{SSA}	0.6	0.4-0.8	higher values cause less extended LGM state and less overshoot
SIA enhancement [ ], E_{SIA}	2	1-5	smaller values cause less extended LGM state and less overshoot
Flow law exponent [ ], q	0.75	0.25-1	smaller values cause less extended LGM state and delayed retreat
Till water decay rate [mm yr^{-1}], T	3	0.5-3	higher values cause slightly less extended LGM
Till effect. overburden [ ], N	0.04	0.02-0.05	higher values cause slightly less extended LGM
Till friction angle min [°], ϕ	2	1-3	relevant for LGM state and hence for overshoot retreat and re-advance
PICO heat exchange [m s^{-1}], g	$1\text{x}10^{-5}$	$1\text{-}3\text{x}10^{-5}$	2nd order influence on LGM state and timing of retreat
PICO overturning [m^{6} kg^{-1} s^{-1}], C	$8\text{x}10^{5}$	$8\text{-}20\text{x}10^{5}$	2nd order influence on LGM state and timing of retreat
Eigen calving [m s], K	$1\text{x}10^{17}$	$1\text{x}10^{16}$-$5\text{x}10^{17}$	relevant for LGM state and initiation of retreat via ice-shelf buttressing

The table shows key model parameters that have been varied as part of our sensitivity study of our ice-sheet model (see Methods). In each case, the value used in the reference simulation is given, as well as the range over which the parameters were varied during the sensitivity study. Also provided is a summary of the impact of each parameter on the model behaviour with respect to the retreat of the grounding line past its present-day location and its subsequent re-advance. See Methods for a detailed discussion of model sensitivities.